



# Gas-phase dehydration of glycerol to acrolein over $\text{Al}_2\text{O}_3$ -, $\text{SiO}_2$ -, and $\text{TiO}_2$ -supported Nb- and W-oxide catalysts



Mariano Massa<sup>a</sup>, Arne Andersson<sup>a,\*</sup>, Elisabetta Finocchio<sup>b</sup>, Guido Busca<sup>b</sup>

<sup>a</sup> Department of Chemical Engineering, Lund University, Chemical Center, P.O. Box 124, SE-221 00 Lund, Sweden

<sup>b</sup> Department of Chemical and Process Engineering, Genova University, P.le Kennedy 1, I-16129 Genova, Italy

## ARTICLE INFO

### Article history:

Received 9 April 2013

Revised 15 July 2013

Accepted 21 July 2013

### Keywords:

Glycerol  
Dehydration  
Acrolein  
Supported niobia  
Supported tungsten oxide  
Supported Nb–W-oxide  
 $\text{Al}_2\text{O}_3$   
 $\text{TiO}_2$   
 $\text{SiO}_2$   
Acidity

## ABSTRACT

Hypothetical monolayer loadings of niobium and tungsten oxide supported on alumina, silica, and titania were investigated as catalysts for the dehydration of glycerol to produce acrolein. Besides activity measurements, to have information about the supported structures, the catalysts were characterized by XRD, Raman spectroscopy, XPS, XANES, and FTIR combined with adsorption of pyridine and  $\text{CO}_2$ . Compared with silica showing the presence of crystalline  $\text{Nb}_2\text{O}_5$  and  $\text{WO}_3$ , alumina and titania gave better dispersion and formation of hydrated niobate and tungstate species. Deactivation of the catalysts occurred with time on stream. However, the stability was improved considerably by adding oxygen to the feed. A dependence of the selectivity to acrolein on the Brønsted acidity of the catalyst was observed. Under anaerobic conditions, an alumina-supported mixed Nb–W-oxide catalyst gave a selectivity of more than 70% for glycerol conversions above 40%. Even better selectivity was obtained using a catalyst with tungsten oxide supported on titania, which gave 80% selectivity under aerobic conditions at high conversion.

© 2013 Elsevier Inc. All rights reserved.

## 1. Introduction

During the last decades, the hike in the petroleum price and the increasing awareness that the oil reservoirs are limited have led to worldwide focus on the use of renewable resources for producing fuels and chemicals [1–3]. For example, cooking oil, tallow, yellow grease, poultry grease, cottonseed oil, rapeseed oil, and soybean oil are extensively converted through transesterification into fatty acid methyl esters (biodiesel). Pure or blended biodiesel can be run in conventional compression-ignition engines, and moreover, the use of biodiesel significantly reduces the emissions to the atmosphere of unburned hydrocarbons, carbon monoxide, particulate matter, sulfur, and carcinogenic compounds [4,5]. It has been reported that the production capacity in the world of biodiesel has increased tremendously from 117 to 1577 million gallons per year during the period from 2009 to 2012 and is thought to rise up to 4.4 billion gallons per year by 2015 [6].

The major challenge in biodiesel production is to find markets for the crude glycerol being formed in large quantity as a major by-product during the transesterification process [7]. Refined glycerol is currently employed in the food and tobacco industries as

well as in the manufacture of cosmetics, pharmaceuticals, and other personal care products [1,8]. The increased production of biodiesel has created a surplus of glycerol on the market. Consequently, the prices of crude and refined glycerol have declined, making glycerol a possible raw material for the manufacture of added-value chemicals via sustainable routes comprising oxidation, reduction, or reaction with other species to form new products [9–12].

One interesting product from glycerol is acrolein, which currently is produced by oxidation of propylene over bismuth molybdate-based catalysts [13,14]. Acrolein is an important intermediate for making acrylic acid, from which acrylates are produced [15]. The double intramolecular dehydration of glycerol into acrolein has widely been investigated in the gas phase over solid acid catalysts. Particularly, zeolites [16–21], heteropolyacids (HPAs) [1,22–31], bulk as well as supported phosphates [32–36], sulfonic-functionalized SBA-15 [37], supported tungsten oxide [38–42], pure  $\text{Nb}_2\text{O}_5$  [43], and supported niobia [41,44–46] have shown promising results. In general, the investigations outline that the activity is strongly dependent on the density of acid sites, whereas the selectivity to acrolein is related to the presence of Brønsted acid sites. Although the activity and the selectivity to acrolein can be optimized by finding the best combination of space velocity, reaction temperature and glycerol/water ratio in the feed, catalyst

\* Corresponding author. Fax: +46 46 149156.

E-mail address: [Arne.Andersson@chemeng.lth.se](mailto:Arne.Andersson@chemeng.lth.se) (A. Andersson).

deactivation is a major issue irrespectively of the catalyst system being used [1,2,14]. In fact, a loss of activity is noticeable already after a few hours on stream (4–12 h) unless excess catalyst (low space velocity) is used. The deactivation has mostly been ascribed to coking and formation of high-boiling compounds. Attempts to regenerate the catalyst have successfully been made by treating the catalyst in air at a temperature between 300 and 550 °C [16,24,26,30,32,41,43,44,47]. Alternatively, it has been found that the deactivation process can be slowed down by having oxygen in the feed [40,41,48–51]. Furthermore, Alhanash et al. [25] report that Cs<sub>2.5</sub>H<sub>0.5</sub>PW<sub>12</sub>O<sub>40</sub> doped with 0.5 wt% Pd gives good catalytic stability and performance when co-feeding glycerol together with hydrogen.

In our previous work, we reported a comprehensive study of Nb-, W-, and NbW-oxides on monoclinic zirconia as catalysts for the dehydration of glycerol to give acrolein [41]. In the present work, we have prepared alumina-, silica-, and titania-supported catalysts containing W-oxide and Nb-oxide separately and in synergy, and tested them in glycerol dehydration under different space velocities. Moreover, the catalysts have been characterized by X-ray diffraction (XRD), Fourier transform Raman spectroscopy (FT-Raman), X-ray photoelectron spectroscopy (XPS), X-ray absorption spectroscopy (XANES), and Fourier transform infrared spectroscopy (FTIR) combined with pyridine and CO<sub>2</sub> adsorption.

## 2. Experimental

### 2.1. Catalyst preparation

The catalysts to be investigated were prepared by incipient wetness impregnation of Al<sub>2</sub>O<sub>3</sub> (Alfa Aesar), SiO<sub>2</sub> (Grace GmbH), and TiO<sub>2</sub> (Alfa Aesar) with solutions containing the desired amount of the active metal precursor. Briefly, a homogeneous water solution of either ammonium paratungstate (NH<sub>4</sub>)<sub>10</sub>(W<sub>12</sub>O<sub>41</sub>)·7H<sub>2</sub>O (Riedel-de Haën), niobium oxalate C<sub>10</sub>H<sub>5</sub>NbO<sub>20</sub> (ABCR), or both salts was added dropwise onto the support particles with diameters in the range 0.250–0.450 mm, which were obtained by pressing, crushing, and sieving pellets. After impregnation, the support was allowed to dry at 90 °C for 30 min. The impregnation and drying procedure were repeated a few times to obtain the desired total loading. Before use of the samples in glycerol dehydration, calcination of the catalyst precursors on Al<sub>2</sub>O<sub>3</sub> and SiO<sub>2</sub> was performed during 6 h at 600 °C. The TiO<sub>2</sub>-supported precursors, on the other hand, were calcined at 450 °C to avoid the anatase–rutile phase transition [52]. The calcination temperature was reached ramping from room temperature with a heating rate of 5 °C/min. The textural properties of the preparations are given in Table 1, where the number preceding Nb and W is the loading in theoretical monolayers of the specific element in the form of oxide, e.g., the notation 1WTi denotes a TiO<sub>2</sub>-supported catalyst with a WO<sub>x</sub> loading of one theoretical monolayer. By a monolayer is meant a hypothetical layer of oxide covering the surface of the support and is defined as 11.6 μmol cations/m<sup>2</sup> of support surface [53]. The catalyst contents of Nb and W in wt% sample and atoms/nm<sup>2</sup> are given in Table S1 (supplement). It should be noted that a theoretical layer does not necessarily have to correspond to a true monolayer and complete dispersion of the supported phase.

The calcined supports are denoted Al<sub>2</sub>O<sub>3</sub>600, SiO<sub>2</sub>600 and TiO<sub>2</sub>450, where the number refers to the calcination temperature.

### 2.2. Catalyst characterization

Multipoint BET measurements were performed on a Micromeritics ASAP 2400 instrument to determine the specific surface area, the pore volume, and the average pore size of both freshly

**Table 1**  
Textural properties of the catalysts before and after use in glycerol dehydration.<sup>a</sup>

Catalyst	Specific surface area (m <sup>2</sup> /g)		Pore size (Å)		Pore volume (cm <sup>3</sup> /g)			
	Fresh <sup>b</sup>	Used <sup>b</sup>	Fresh <sup>c</sup>	Used <sup>c</sup>	Fresh	Used		
Al <sub>2</sub> O <sub>3</sub>	100	–	100	–	178	–	0.48	–
Al <sub>2</sub> O <sub>3</sub> 600	100	93	100	93	180	177	0.45	0.41
1NbAl	97	77	113	89	150	129	0.36	0.25
1WAl	81	69	104	88	170	143	0.34	0.25
0.25Nb0.75WAl	79	73	100	93	178	149	0.35	0.27
0.5Nb0.5WAl	81	82	101	102	170	136	0.34	0.28
0.75Nb0.25WAl	101	81	121	97	148	129	0.37	0.26
SiO <sub>2</sub>	95	–	95	–	500	–	0.94	–
SiO <sub>2</sub> 600	99	91	99	91	415	429	1.02	0.98
1NbSi	82	66	94	76	387	411	0.79	0.68
1WSi	81	73	102	92	415	416	0.84	0.76
0.25Nb0.75WSi	84	73	106	91	395	425	0.83	0.77
0.5Nb0.5WSi	77	79	95	97	427	390	0.82	0.77
0.75Nb0.25WSi	83	76	99	91	393	379	0.81	0.72
TiO <sub>2</sub>	150	–	150	–	105	–	0.39	–
TiO <sub>2</sub> 450	100	64	100	64	140	154	0.34	0.25
1NbTi	110	36	136	45	86	118	0.23	0.11
1WTi	114	56	161	79	103	107	0.29	0.15
0.25Nb0.75WTi	96	48	136	68	101	109	0.24	0.13
0.5Nb0.5WTi	92	38	128	53	93	111	0.21	0.11
0.75Nb0.25WTi	108	37	144	50	93	122	0.25	0.11

<sup>a</sup> After 4-h glycerol dehydration at 305 °C. Amount catalyst: 0.8 g. Feed: 3.6 ml/h 20 wt% aqueous glycerol vaporized in 15 ml/min Ar. Glycerol WHSV: 0.94 h<sup>-1</sup>.

<sup>b</sup> Specific surface area expressed per mass of catalyst.

<sup>c</sup> Specific surface area expressed per mass of support.

prepared and used catalysts. The samples were degassed for 24 h at 100 °C under vacuum before the measurement.

Powder X-ray diffraction analysis was performed on a Seifert XRD 3000 TT diffractometer using Cu Kα radiation and a rotating sample holder. The tube voltage and the current were set to 40 kV and 40 mA, respectively. The instrument was calibrated using a Si standard. Diffraction patterns were recorded between 5° and 80° 2θ with a step width of 0.05° (10 s/step).

Raman spectra were recorded on a Bruker IFS 66 FTIR spectrometer equipped with a Bruker FRA 106 FT-Raman device, an Nd:YAG laser, and a germanium diode detector. The spectra were taken under ambient conditions at 180° backscattering. In each measurement, 1000 scans were averaged with the resolution 4 cm<sup>-1</sup>.

Infrared measurements (100 scans, 4 cm<sup>-1</sup> resolution) were made in transmission mode under static conditions using a Nicolet Magna 750 Fourier transform instrument and a conventional IR cell connected to a gas manipulation apparatus. The samples to be analyzed were pressed into discs (30–40 mg, 2 cm<sup>2</sup> disc size). After treating the sample at 500 °C or 450 °C for the samples with TiO<sub>2</sub> for 30 min under vacuum (10<sup>-5</sup> torr), a spectrum of the sample was recorded. Then, adsorption of CO<sub>2</sub> (50 torr) and pyridine (10 torr) was performed at room temperature in order to determine the occurrence of basic and acidic sites, respectively. IR spectra of adsorbed CO<sub>2</sub> and pyridine were recorded both immediately after evacuation and again after outgassing for 30 min. For quantification of Brønsted (BAS) and Lewis (LAS) acidic sites, additional spectra were recorded again after heating the sample at 110 °C. The concentrations of BAS and LAS acidic sites were determined using the method proposed by Emeis [54].

XANES measurements were carried out at the I811 station in Maxlab at Lund University. The beamline is equipped with three ionization chambers and a Si (311) crystal monochromator. W L<sub>1</sub> and Nb K-edge spectra were recorded in fluorescence mode using W (12099.88 eV) and Nb (18982.97 eV) metal foils, respectively, as energy references and a passivated implanted planar silicon (PIPS) detector positioned perpendicular to the incoming beam. The reference foils were placed before the third ionization

chamber, whereas the sample to be analyzed was in between the first and the second ionization chambers. Zr and Ge metal foils were used for the recording of the Nb- and W-edge, respectively, to filter off the fluorescence contribution from the support and other elements. For the measurements, the samples were ground and diluted with boron nitride to obtain an optimal absorption signal.

XPS analysis was made on a PHI 5500 instrument with MgK $\alpha$  radiation (1253.6 eV). For the measurements, powder samples, which were obtained by grinding the catalysts, were placed on a sticky and conducting tape. Charging effects were reduced using a flood gun, submitting low-energy electrons from a W-filament to the sample. The electron flow was adjusted until the C 1s peak position was at 285.0 eV, which binding energy was used as energy reference. Quantifications were made using a Shirley function for the background.

### 2.3. Activity measurements

The dehydration of glycerol was studied at atmospheric pressure in a vertical stainless steel reactor of 25 cm length and 0.4 cm internal diameter, where the catalyst sample was placed in the middle on glass wool support. To obtain isothermal conditions, the reactor was closely fixed in an aluminum block, which was surrounded by glass wool and a shield of aluminum foil. Moreover, the aluminum block was equipped with two cartridge heaters and a thermocouple positioned nearby the catalytic bed to control the temperature.

Ar was used as carrier gas for glycerol. The Ar flow was controlled by a Bronkhorst mass flow controller set to 15 ml/min. After passing a first pre-heating section held at 330 °C, the carrier gas was directed to a vaporization section where 3.6 ml/h of 20 wt% aqueous glycerol solution (0.0082 mol glycerol/h and 0.167 mol H<sub>2</sub>O/h) was injected by a Kd Scientific pump and became quickly vaporized at 280 °C. The resulting gas mixture with the molar ratios Ar/glycerol/H<sub>2</sub>O = 5:1:21 then passed a second pre-heater kept at 310 °C before entering the reactor. Unless otherwise specified, the reactor was loaded with 0.8 g catalyst and the reaction temperature was 305 °C.

After 3 h reaction, reaction products and unconverted glycerol were collected during 1 h in an ice trap with three condensers in series. To the condensed products, n-butanol was added as internal standard, and the obtained solution was analyzed on a Varian Star 3400 gas chromatograph equipped with a 10 wt% FFAP/Chromosorb W-AW column (2 mm i.d., 2.5 m long) and an FID detector. To obtain effective product separation, the column was held at 50 °C during 4 min before raising the temperature 14 °C/min from 50 up to 250 °C, where it was kept for 20 min. CO and CO<sub>2</sub> were analyzed online on a Hiden HPR 20 mass spectrometer. For the latter purpose, the outlet flow from the condensers was mixed with 20 ml/min Ar. Blank tests without catalyst showed negligible conversion (<1%) of glycerol.

Glycerol conversion, product selectivity, and the carbon balance were calculated as follows using calibration curves with n-butanol as internal standard for glycerol and each product:

Glycerol conversion (%)

$$= \frac{\text{mole glycerol pumped} - \text{mole unconverted glycerol}}{\text{mole glycerol pumped}} \times 100$$

Product selectivity (%)

$$= \frac{\text{mole carbon in the product}}{\text{mole carbon in converted glycerol}} \times 100$$

Carbon balance (%)

$$= \text{sum of the selectivities to identified products}$$

Selectivity to unidentified products (%)

$$= 100 - \text{Carbon balance}$$

## 3. Results

### 3.1. BET

The textural properties of the freshly prepared and the used catalysts and supports are listed in Table 1. Clearly, the pure Al<sub>2</sub>O<sub>3</sub> and SiO<sub>2</sub> supports show practically unchanged specific surface area after being calcined at 600 °C, whereas the TiO<sub>2</sub> sinters at the calcination temperature 450 °C. Compared with the pure Al<sub>2</sub>O<sub>3</sub> and SiO<sub>2</sub> supports, the corresponding samples with Nb and W generally show lower specific surface areas expressed per g catalyst but rather unchanged or higher values when expressed per g support. Regarding the preparations on TiO<sub>2</sub>, the presence of Nb and W turns out to stabilize the support toward sintering during the calcination, as indicated by the fact that the supported samples have surface area values in m<sup>2</sup>/g support that are in-between the values for the as-received and the calcined TiO<sub>2</sub>. After being subjected to glycerol dehydration for 4 h, the specific surface areas and the pore volumes of the catalysts are noticeably reduced in most cases.

### 3.2. XRD

Figs. 1–3 show the diffraction patterns of freshly prepared catalysts and calcined supports. The powder patterns recorded after use of the catalysts in glycerol dehydration were very similar to those for the unused samples and are therefore not shown.

The XRD patterns of the calcined Al<sub>2</sub>O<sub>3</sub> and the Al<sub>2</sub>O<sub>3</sub>-supported catalysts are presented in Fig. 1. The calcined Al<sub>2</sub>O<sub>3</sub> exhibits the

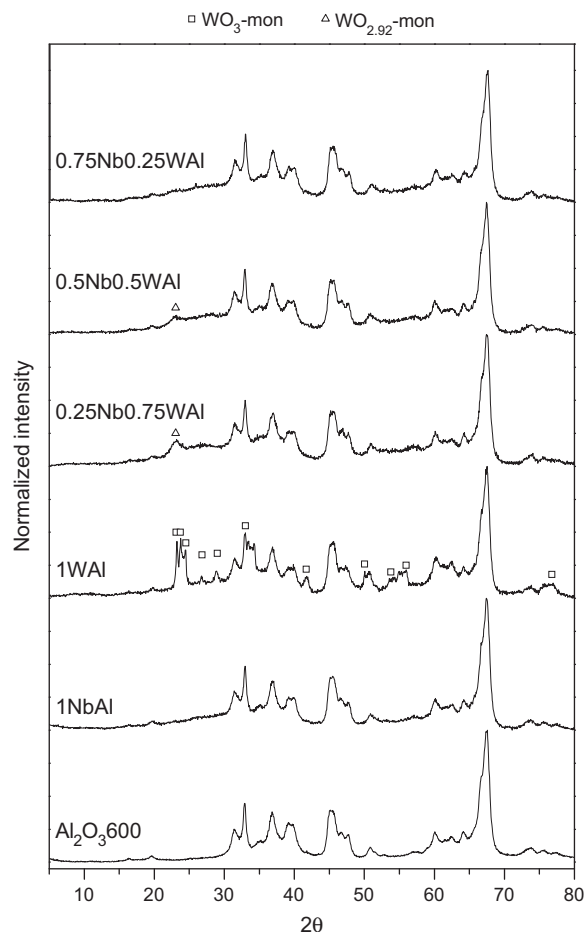
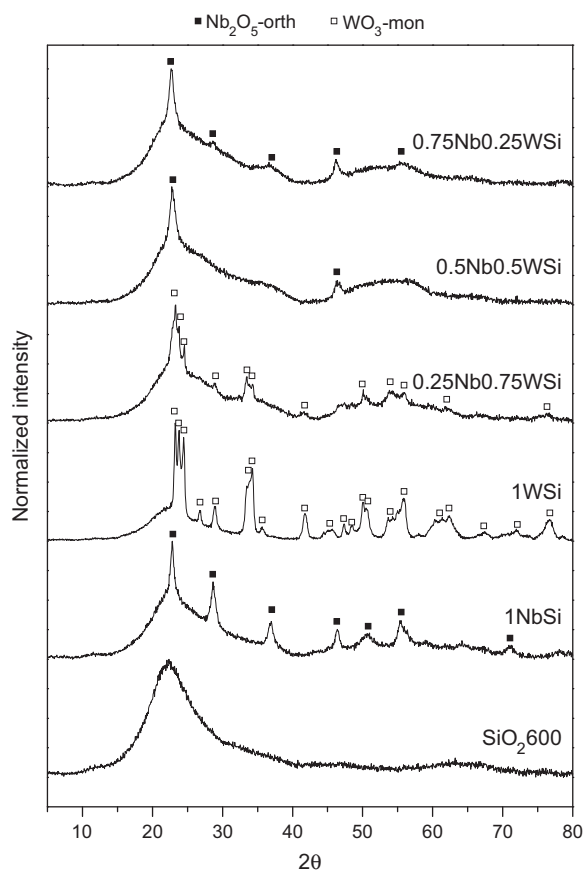
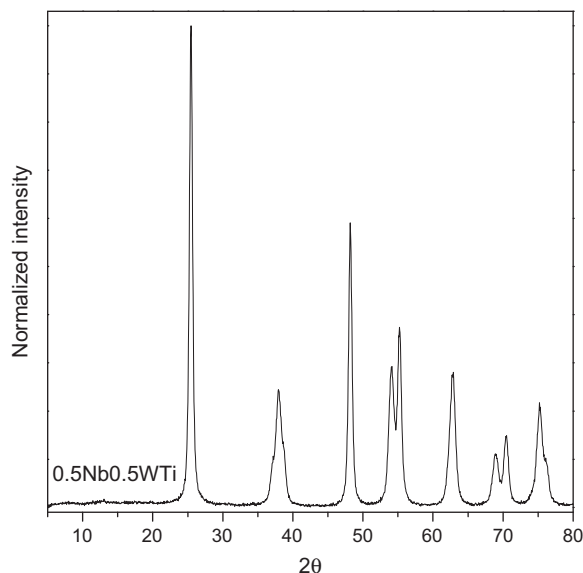


Fig. 1. Normalized XRD patterns of the calcined alumina support (Al<sub>2</sub>O<sub>3</sub>600) and freshly prepared Al<sub>2</sub>O<sub>3</sub>-supported catalysts.



**Fig. 2.** Normalized XRD patterns of the calcined silica support ( $\text{SiO}_2$ 600) and freshly prepared  $\text{SiO}_2$ -supported catalysts.



**Fig. 3.** Normalized XRD pattern for 0.5Nb0.5WTi.

typical peaks from  $\theta$ - $\text{Al}_2\text{O}_3$  (JCPDS file no. 01-1304) [55], which was also the case for the as-received support. For the 1WAl sample with a tungsten oxide loading of one theoretical monolayer, diffraction peaks from monoclinic  $\text{WO}_3$  are observed (JCPDS file no. 43-1035) [55] in addition to the peaks from the support. On the other hand, in the diffractogram of the corresponding niobia sample

1NbAl, only peaks from  $\theta$ - $\text{Al}_2\text{O}_3$  appear, indicating better dispersion on the alumina of niobia as compared to tungsten oxide. However, the formation of some X-ray amorphous niobia cannot be excluded. Considering the samples with both Nb and W, besides the peaks from the support, a peak is seen at  $23.2^\circ 2\theta$ , whose intensity decreases with increasing Nb/W ratio and is almost absent in the diffractogram of 0.75Nb0.25WAl. This peak, as will be explained in the Discussion in Section 4.1, possibly can be assigned to the strongest peak of monoclinic  $\text{WO}_{2.92}$  (JCPDS file no. 30-1387) [55].

Fig. 2 displays the XRD patterns of the  $\text{SiO}_2$ -supported catalysts and the calcined support. Both the diffractogram of the  $\text{SiO}_2$  as-received (not shown) and that of the calcined sample show a very broad peak at  $22^\circ 2\theta$ . For 1WSi and 0.25Nb0.75WSi, the XRDs show the formation of monoclinic  $\text{WO}_3$  (JCPDS file no. 1-75-2072) [55] on the support, whereas XRD analysis of 1NbSi, 0.75Nb0.25WSi, and 0.5Nb0.5WSi reveals the presence orthorhombic  $\text{Nb}_2\text{O}_5$  (JCPDS file no. 30-873) [55].

The diffractograms of the  $\text{TiO}_2$ -supported samples display no peaks from Nb- and W-oxides. Only peaks from the anatase polymorph of  $\text{TiO}_2$  (JCPDS file no. 1-75-2552) [55] are observed, as exemplified in Fig. 3 by the XRD for the 0.5Nb0.5WTi catalyst.

### 3.3. Raman spectroscopy

The Raman spectra of the freshly prepared  $\text{Al}_2\text{O}_3$ -,  $\text{SiO}_2$ -, and  $\text{TiO}_2$ -supported catalysts are displayed in Figs. 4–6, respectively. All spectra were recorded at room temperature under ambient conditions. Regarding the preparations on  $\text{Al}_2\text{O}_3$ , the Raman spectra were characterized by a broad feature typical of the support, which consequently prevented us from discerning additional features. Only in case of the 1WAl sample, some spectral features not belonging to the alumina were observed. The spectrum in Fig. 4 for 1WAl shows two bands at 805 and 715  $\text{cm}^{-1}$ , which are from monoclinic  $\text{WO}_3$  as a comparison with the spectrum in Fig. 5 for the latter phase shows. Additionally, there is a band at  $\sim 973 \text{ cm}^{-1}$  from a hydrated polytungstate species interacting with the support [56,57].

Fig. 5 depicts the Raman spectra of the pure calcined silica support ( $\text{SiO}_2$ 600), pure orthorhombic  $\text{Nb}_2\text{O}_5$ , pure monoclinic  $\text{WO}_3$ , and the silica-supported catalysts with  $\text{NbO}_x$  and  $\text{WO}_x$ . The

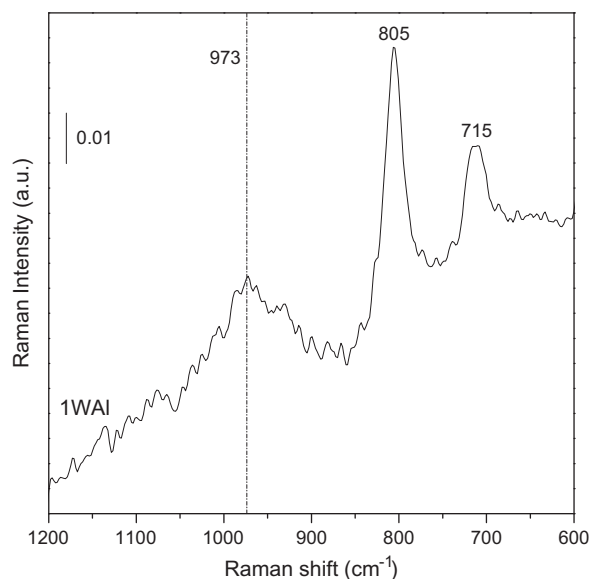


**Fig. 4.** The Raman spectrum for 1WAl is shown after subtraction of the contribution from alumina. Both spectra were recorded at ambient conditions.

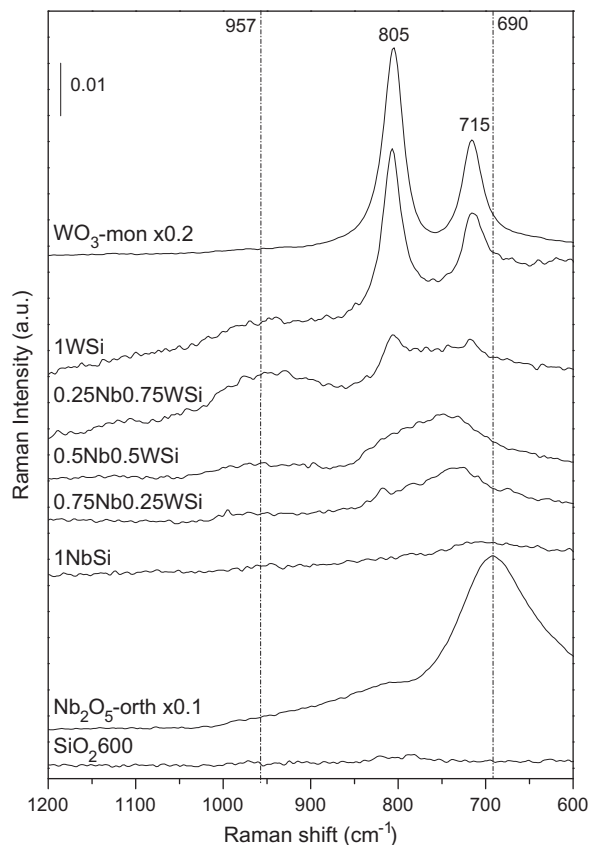


**Fig. 5.** Raman spectra recorded at ambient conditions of the calcined silica support (SiO<sub>2</sub>600) and the freshly prepared SiO<sub>2</sub>-supported catalysts. The spectra of pure monoclinic WO<sub>3</sub> and pure orthorhombic Nb<sub>2</sub>O<sub>5</sub> are included for comparison.

calcined silica is featureless in the region displayed, whereas the deposition of NbO<sub>x</sub> and WO<sub>x</sub> gives rise to a number of bands, some of which being rather weak as revealed by the relatively high noise/signal ratio. In the spectrum for 1NbSi, a weak band characteristic of orthorhombic Nb<sub>2</sub>O<sub>5</sub> [41,58] is noticeable at 690 cm<sup>-1</sup>. However, the band is obscured by another band at higher wavenumber, which position shifts from 720 cm<sup>-1</sup> to 760 cm<sup>-1</sup> with decreasing Nb-content from 1NbSi to 0.25Nb0.75WSi. Concurrently, the intensity of the band increases significantly and is the highest for 0.5Nb0.5WSi. In the spectrum for 1WSi, there are two strong bands at 805 and 715 cm<sup>-1</sup> from monoclinic WO<sub>3</sub> [41,56], which bands also appear in the spectrum for 0.25Nb0.75WSi. Moreover, all NbWO<sub>x</sub>/SiO<sub>2</sub> catalysts as well as 1WSi exhibit a weak and broad band around 960 cm<sup>-1</sup>, whose intensity increases with increasing tungsten content from 0.75Nb0.25WSi up to 0.25Nb0.75WSi. The same band has been observed also in previous investigations of silica-supported WO<sub>x</sub> [56,59–61] and has been assigned to a hydrated polytungstate structure [56,62].

In agreement with the XRD results (Fig. 3), the Raman spectrum of the calcined titania support (TiO<sub>2</sub>450) exhibited distinct Raman modes characteristic of anatase at 145, 200, 395, 515, and 639 cm<sup>-1</sup> (not shown) [63,64]. Additionally, as seen in Fig. 6, there is a broad and poorly visible band located at about 798 cm<sup>-1</sup>, which is the first overtone of the anatase band at 395 cm<sup>-1</sup> [65–67]. Although the anatase feature is maintained after deposition of W- and Nb-oxides, new spectral components arise owing to surface oxide species. In fact, in the spectrum of 1NbTi in Fig. 6, there is a weak broadband around 910 cm<sup>-1</sup> from hydrated NbO<sub>x</sub> surface species [66,68,69]. Besides the contribution from the support, the Raman spectrum of 1WTi in Fig. 6 shows a distinct band at

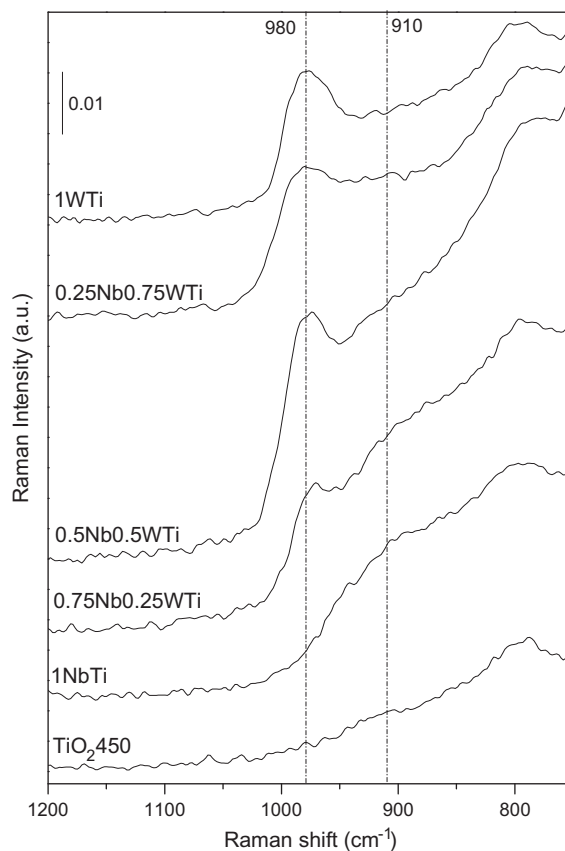


**Fig. 6.** Raman spectra recorded under ambient conditions of the calcined titania support (TiO<sub>2</sub>450) and the freshly prepared TiO<sub>2</sub>-supported catalysts.

980 cm<sup>-1</sup>, which can be assigned to a hydrated polytungstate surface structure [70,71]. The Raman spectra of the NbWO<sub>x</sub> catalysts combine in correspondence with their Nb/W ratios the features of the 1NbTi and 1WTi spectra, showing a broadband from a niobium oxide species around 900 cm<sup>-1</sup> and a distinct peak in the 975–980 cm<sup>-1</sup> region from surface polytungstate. It is worth noting that the latter band increases in intensity and shifts from 971 cm<sup>-1</sup> for 0.75Nb0.25WTi to 980 cm<sup>-1</sup> for 0.25Nb0.75WTi and 1WTi in agreement with previous observations [70,71].

### 3.4. XPS surface analysis

In order to investigate the composition and the oxidation states of W and Nb at the support surface, XPS measurements were performed. In Table 2 are the binding energies reported that were determined for the W 4f<sub>7/2</sub> and Nb 3d<sub>5/2</sub> peaks in the fresh samples. The fact that the binding energies fall in the ranges 35.8–36.6 eV and 207.2–207.8 eV indicates the presence of W<sup>6+</sup> and Nb<sup>5+</sup> species, respectively, at the surface of the supports. In fact, the corresponding values for reduced W- and Nb-oxide species fall well below 35.0 and 206.5 eV, respectively [72].

For the samples with either Nb or W, the quantitative data in Table 3 show for all supports better dispersion of Nb than of W. Moreover, the dispersion decreases in the order TiO<sub>2</sub> > Al<sub>2</sub>O<sub>3</sub> > SiO<sub>2</sub>. For the samples with both Nb and W, the behavior is different in that the co-presence of these elements considerably improves the dispersion of both. As indicated by the data in Table 3, the mixed Nb–W-oxide samples on TiO<sub>2</sub> and Al<sub>2</sub>O<sub>3</sub> have better total dispersion of W and Nb than is the case on SiO<sub>2</sub>.

### 3.5. XANES

To have more information about the coordination environment and the valence of tungsten and niobium at the surface of the supports, XANES spectra were recorded. The normalized Nb K and W L<sub>1</sub> absorption edges for the freshly prepared samples with one theoretical layer of Nb- and W-oxides are shown in Fig. 7 along with reference spectra for orthorhombic Nb<sub>2</sub>O<sub>5</sub>, monoclinic Nb<sub>2</sub>O<sub>5</sub>, and monoclinic WO<sub>3</sub>. Spectra for the remaining fresh samples and those for the used ones are not shown as they were nearly identical to the spectra in Fig. 7.

In the Nb K-edge XANES spectra in Fig. 7a, two features are distinguishable, namely an edge and a pre-edge. The position of the main-edge absorption, which is due to 1s → 5p electron transitions, is strictly related to the formal valence of the element [73]. The spectra in Fig. 7a clearly show that the main-edge position ( $E_0$ ), corresponding to the first inflection point of the absorption, is very similar for the supported catalysts 1NbAl, 1NbSi, and 1NbTi. Moreover, the position ( $E_0 = 18,998$  eV) agrees with that for monoclinic and orthorhombic Nb<sub>2</sub>O<sub>5</sub>, indicating that the supported niobium is pentavalent on all supports. Concerning the pre-edge feature, originating from the 1s → 4d electron transition, it is sensitive to the coordination around niobium [73]. In fact, for perfect octahedral symmetry, the pre-edge feature is missing, and the area of the pre-peak increases with increased displacement from the center [74]. Considering the pre-peak intensities for the samples in Fig. 7a, it is seen that the supported catalysts give pre-peak intensities in between those for the orthorhombic and monoclinic Nb<sub>2</sub>O<sub>5</sub> phases. In the former structure, the Nb atoms are in both octahedral and pentagonal bipyramidal coordination with Nb–O distances in the range 1.77–2.19 Å [75], whereas in the latter phase, they have octahedral coordination with bond distances varying between 1.73 and 2.31 Å [76]. Thus, based on the pre-edge intensity values, it can be proposed that the supported niobia have essentially distorted octahedral coordination.

Similar to Nb in niobia, the valence and the coordination of W in tungsten oxides are determined by the position of the W L<sub>1</sub>-edge (threshold energy) and by the intensity of the pre-peak absorption, respectively [77]. The latter absorption is due to the 2s → 5d transition, which is dipole-forbidden in the case W being in perfect octahedral symmetry (absence of pre-edge). However, the transition is allowed for the distorted octahedral (shoulder-like pre-edge) and tetrahedral (intense pre-edge peak) symmetries due to the mixing of tungsten d orbitals with oxygen p orbitals [77–80]. The spectra in Fig. 7b show that the W L<sub>1</sub>-edge position for the supported samples with monolayer loading of WO<sub>x</sub> is fairly close to that for the monoclinic WO<sub>3</sub> reference ( $E_0 = 12,105$  eV), suggesting that tungsten is hexavalent on the supports. Furthermore, the fact that the pre-peak appears as a shoulder at the low energy side of the W L<sub>1</sub>-edge indicates that tungsten on the supports is in a distorted octahedral coordination likewise in the reference compound monoclinic WO<sub>3</sub> [81]. Tungsten in tetrahedral coordination, e.g., BaWO<sub>4</sub> [78], Na<sub>2</sub>WO<sub>4</sub> [77,79] and Al<sub>2</sub>WO<sub>4</sub> [80], gives a much more intense and well resolved pre-peak.

**Table 2**

Binding energy of W 4f<sub>7/2</sub> and Nb 3d<sub>5/2</sub> as determined by XPS for the Al<sub>2</sub>O<sub>3</sub>-, SiO<sub>2</sub>- and TiO<sub>2</sub>-supported catalysts.

Catalyst	Binding energy (eV)		Catalyst	Binding energy (eV)		Catalyst	Binding energy (eV)	
	W	Nb		W	Nb		W	Nb
1NbAl	–	207.5	1NbSi	–	207.8	1NbTi	–	207.3
1WAl	36.6	–	1WSi	36.0	–	1WTi	35.9	–
0.25Nb0.75WAl	36.0	207.4	0.25Nb0.75WSi	35.8	207.2	0.25Nb0.75WTi	35.8	207.3
0.5Nb0.5WAl	35.9	207.4	0.5Nb0.5WSi	35.9	207.4	0.5Nb0.5WTi	35.8	207.4
0.75Nb0.25WAl	35.9	207.4	0.75Nb0.25WSi	35.9	207.4	0.75Nb0.25WTi	35.9	207.5

**Table 3**

Surface compositions (at.%) for the Al<sub>2</sub>O<sub>3</sub>-, SiO<sub>2</sub>-, and TiO<sub>2</sub>-supported Nb- and W-oxide catalysts as determined by XPS.

Catalyst	Nb	W <sup>a</sup>	Al	Si	Ti	O
1NbAl	6.6	0.0	30.5			62.9
1WAl	0.0	3.3	32.8			63.9
0.25Nb0.75WAl	4.7	10.4	17.9			67.1
0.5Nb0.5WAl	10.3	10.2	10.6			68.8
0.75Nb0.25WAl	10.0	3.9	20.5			65.6
1NbSi	1.0	0.0		32.0		67.0
1WSi	0.0	0.4		32.6		67.0
0.25Nb0.75WSi	1.7	4.3		26.1		67.9
0.5Nb0.5WSi	2.0	3.1		27.7		67.2
0.75Nb0.25WSi	2.1	1.4		29.3		67.2
1NbTi	11.3	0.0			16.2	72.4
1WTi	0.0	5.0			22.5	72.5
0.25Nb0.75WTi	5.1	12.1			8.5	74.3
0.5Nb0.5WTi	7.5	8.5			10.3	73.7
0.75Nb0.25WTi	4.2	2.5			21.2	72.2

<sup>a</sup> Calculated using the W 4f<sub>7/2</sub> peak for the Al<sub>2</sub>O<sub>3</sub>- and SiO<sub>2</sub>-supported catalyst, whereas the W 4d<sub>5/2</sub> peak was used in case of the TiO<sub>2</sub>-supported samples due to the overlap between the W 4f and the Ti 2p signals.

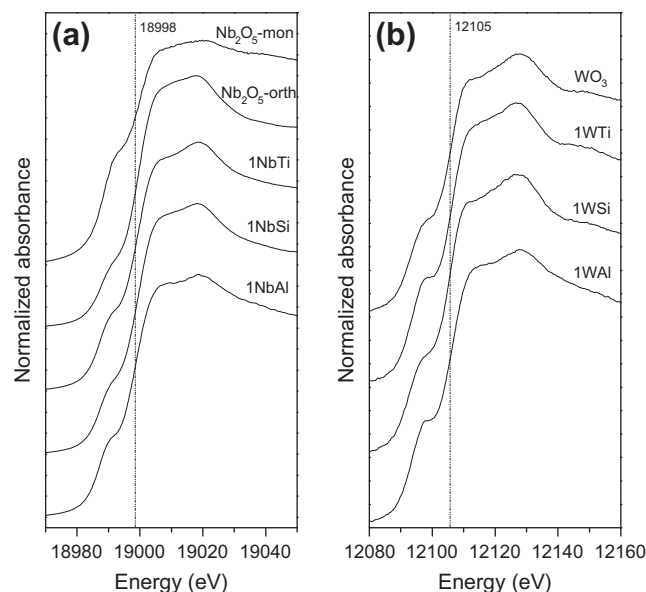


**Fig. 7.** Near-edge X-ray absorption spectra of: (a) Nb K for the freshly prepared catalysts with one theoretical layer of NbO<sub>x</sub>, orthorhombic Nb<sub>2</sub>O<sub>5</sub> and monoclinic Nb<sub>2</sub>O<sub>5</sub>, and (b) W L<sub>1</sub> for the freshly prepared catalysts with one theoretical layer of WO<sub>x</sub> and monoclinic WO<sub>3</sub>.

### 3.6. Activity measurements

The catalytic performances of the catalysts in the dehydration of glycerol are given in Table 4. It is seen that the Al<sub>2</sub>O<sub>3</sub> support although active is not very selective to acrolein (38%). However,

**Table 4**  
Catalytic performance of Nb-, W-, and NbW-oxide supported on Al<sub>2</sub>O<sub>3</sub>, SiO<sub>2</sub>, and TiO<sub>2</sub> in the dehydration of glycerol.<sup>a</sup>

Catalyst	Glycerol conversion (%)	Selectivity to products (%)								CO <sub>2</sub>	CO	Carbon balance (%)
		Acetaldehyde	Propionaldehyde	Acetone	Acrolein	Allyl Alcohol	Hydroxyacetone	1,2-Propanediol				
Al <sub>2</sub> O <sub>3</sub> 600	98.4	1.4	–	–	38.0	2.0	17.9	0.6	–	0.1	60.1	
1NbAl	97.1	2.1	1.6	0.7	59.9	0.7	13.4	–	–	1.1	80.1	
1WAl	98.6	1.3	1.3	0.3	67.0	0.3	8.0	–	–	1.7	80.4	
0.25Nb0.75WAl	100	2.4	1.6	0.3	70.4	0.6	8.9	–	–	0.2	84.4	
0.5Nb0.5WAl	100	2.7	1.8	0.7	71.9	0.7	11.9	–	–	0.2	89.9	
0.75Nb0.25WAl	100	2.9	1.9	0.9	69.3	0.6	10.3	–	–	0.2	86.1	
SiO <sub>2</sub> 600	1.3	–	–	–	–	–	–	–	23.1	69.2	92.3	
1NbSi	82.0	–	2.4	1.3	57.2	1.1	4.2	–	–	1.8	68.1	
1WSi	28.2	1.1	0.7	–	49.3	2.5	4.6	–	–	4.6	64.5	
0.25Nb0.75WSi	98.7	1.2	0.5	0.3	38.7	1.6	6.0	0.2	–	0.1	48.6	
0.5Nb0.5WSi	99	1.6	0.7	0.5	46.8	1.7	8.0	0.2	–	0.1	59.6	
0.75Nb0.25WSi	98.7	1.2	0.5	0.3	38.7	1.6	6.0	0.2	–	0.1	48.6	
TiO <sub>2</sub> 450	98.9	5.5	5.7	9.4	14.0	1.7	0.9	9.9	–	5.1	53.7	
1NbTi	98.9	2.4	5.7	6.4	55.4	0.5	0.3	0.8	–	3.3	75.5	
1WTi	100	2.5	4.8	4.8	66.2	0.2	–	–	–	2.9	81.9	
0.25Nb0.75WTi	98.8	1.3	3.1	2.6	65.2	0.4	0.2	–	–	2.5	75.8	
0.5Nb0.5WTi	99.3	1.6	3.7	3.5	59.5	0.3	0.1	–	–	2.9	72.6	
0.75Nb0.25WTi	99.3	1.7	4.3	4.4	55.3	0.4	–	–	–	3.3	70.1	

<sup>a</sup> Reaction temperature: 305 °C. Amount catalyst: 0.8 g. Feed: 3.6 ml/h 20 wt% aqueous glycerol vaporized in 15 ml/min Ar. Glycerol WHSV (g glycerol/hr)/(g catalyst): 0.94 h<sup>-1</sup>. Products were collected for 1 h after 3-h operation.

deposition of Nb- and W-oxides on the surface noticeably increases the selectivity to acrolein. Particularly, the catalysts with W give a selectivity to acrolein around 70% at almost complete conversion, whereas 1NbAl with NbO<sub>x</sub> only is less selective (~60%). Except acrolein, hydroxyacetone and small amounts of acetaldehyde, propionaldehyde, acetone, allyl alcohol, 1,2-propanediol, and CO<sub>x</sub> are formed. However, the carbon balance is incomplete and amounts to 60% for the pure Al<sub>2</sub>O<sub>3</sub> and 80–90% for the Al<sub>2</sub>O<sub>3</sub>-supported catalysts.

Concerning silica, the data in Table 4 show that the pure calcined support has almost no activity, producing mainly CO<sub>x</sub>. On silica, the most active samples are those containing both W and Nb. In fact, the activity increases in the following order 1WSi < 1NbSi < 0.25Nb0.75WSi ≈ 0.5Nb0.5WSi ≈ 0.75Nb0.25WSi. It is worth pointing out that the selectivity to acrolein does not follow the same trend. Here, the data are somewhat scattered but are in the range 39–49% except for 1NbSi, giving about 57% selectivity to acrolein. Generally, the carbon balance for the SiO<sub>2</sub>-supported samples is poor and is in the range 49–68%.

All preparations with TiO<sub>2</sub> are active for glycerol dehydration (Table 4). The pure calcined TiO<sub>2</sub> is scarcely selective to acrolein, whereas the best selectivity values are obtained for the catalysts containing tungsten with 1WTi and 0.25Nb0.75WTi being the best giving a selectivity to acrolein of about 65%. Compared with the Al<sub>2</sub>O<sub>3</sub>- and SiO<sub>2</sub>-supported samples, the TiO<sub>2</sub>-supported samples give less hydroxyacetone and more of acetone and propionaldehyde. The carbon balance, however, is incomplete and is in the range 70–82% for the samples with Nb- and W-oxides.

To gain information about catalyst stability, activity testing was performed during 20-h operation of the catalyst. Compared with the results in Table 4 for the space velocity (WHSV) 0.94 h<sup>-1</sup>, the stability tests were performed at the space velocity 2.54 h<sup>-1</sup>, which was obtained by reducing the amount of catalyst from 0.8 g to 0.3 g. The best performing catalyst compositions 0.5Nb0.5WAl and 1WTi on alumina and titania, respectively, were selected for testing. No SiO<sub>2</sub>-supported catalyst was chosen for further testing due to the poor performance to acrolein. Plots of the conversion and the selectivities to acrolein, by-products, and unidentified compounds are displayed in Fig. 8 as a function of time on stream. Fig. 8a shows that the conversion of glycerol on 0.5Nb0.5WAl

decreases from 98% to 41% during 20 h on stream and does not affect the selectivity to acrolein, which remains nearly constant around 74%. Also, the selectivities to other products do not change much with time. Compared with 0.5Nb0.5WAl, the 1WTi catalyst (Fig. 8b) deactivates more severely. During 20-h operation, the conversion drops from 97% to 6%. Simultaneously, the selectivity to acrolein decreases from 72% to 55%, while that to unidentified compounds increases from 16% to ~30%.

To study the effect of oxygen addition to the feed of glycerol, the 0.5Nb0.5WAl and 1WTi catalysts were tested for 20 h under aerobic conditions and at a glycerol WHSV of 2.54 h<sup>-1</sup>. The results are depicted in Fig. 9a and b for 0.5Nb0.5WAl and 1WTi, respectively. Clearly, the addition of oxygen to the feed noticeably improves the stability of the catalyst. For 0.5Nb0.5WAl, the conversion of glycerol slowly decreases from 99% to 96% during 20 h on stream. Concurrently, the selectivity to acrolein decreases from about 70% down to 65%. For 1WTi at the same space velocity, the glycerol conversion remains at about 99% for 20 h on stream, and the selectivity to acrolein increases from 74% to 80%. With oxygen in the feed, acetaldehyde instead of hydroxyacetone turns out to be one of the main by-products together with CO<sub>x</sub> and unidentified products.

To further investigate the stability of the catalysts under aerobic conditions, the glycerol WHSV was increased to 7.55 h<sup>-1</sup> by simply reducing the catalyst amount to 0.1 g. Fig. 10 depicts the changes in glycerol conversion and selectivities to products as a function of time on stream. For 0.5Nb0.5WAl, the decrease in conversion from 81% to 42% is accompanied by a drop in the selectivity to acrolein from 56% to 43% and an increase in the selectivity to unidentified products and CO<sub>x</sub>. In case of 1WTi, the conversion decreases from 96% to 79%, whereas the product distribution remains rather constant with a selectivity to acrolein of about 80%.

### 3.7. Infrared spectroscopy

#### 3.7.1. Investigation of the OH stretching region

Fig. 11 displays FTIR spectra of the calcined supports and the 0.5Nb0.5W catalysts after outgassing. The spectrum of the TiO<sub>2</sub> support shows in the OH stretching region two comparatively weak main bands at 3710 and 3668 cm<sup>-1</sup> with minor components

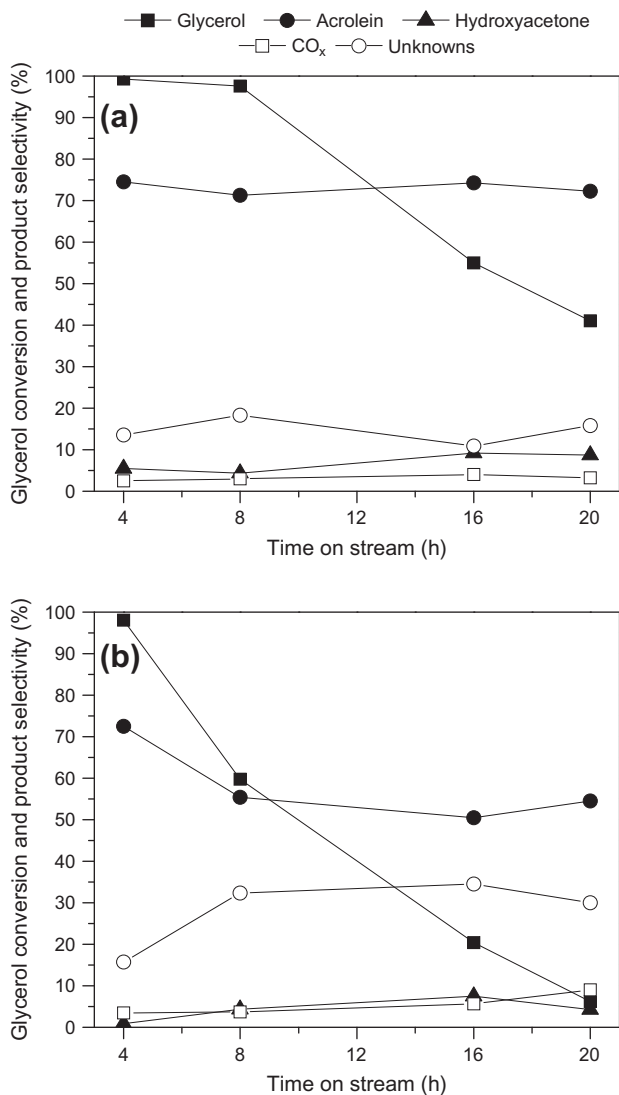


**Fig. 8.** Glycerol conversion (■) and selectivities to acrolein (●), hydroxyacetone (▲), CO<sub>x</sub> (□) and unknowns (○) as a function of time on stream (TOS) for (a) 0.5Nb0.5WAl and (b) 1WTi at 305 °C. Amount catalyst: 0.3 g. Feed: 3.6 ml/h 20 wt% aqueous glycerol vaporized in 15 ml/min Ar. Glycerol WHSV: 2.54 h<sup>-1</sup>. Small amounts of acetaldehyde, propionaldehyde, acetone, allyl alcohol, and 1,2-popanediol were also formed.

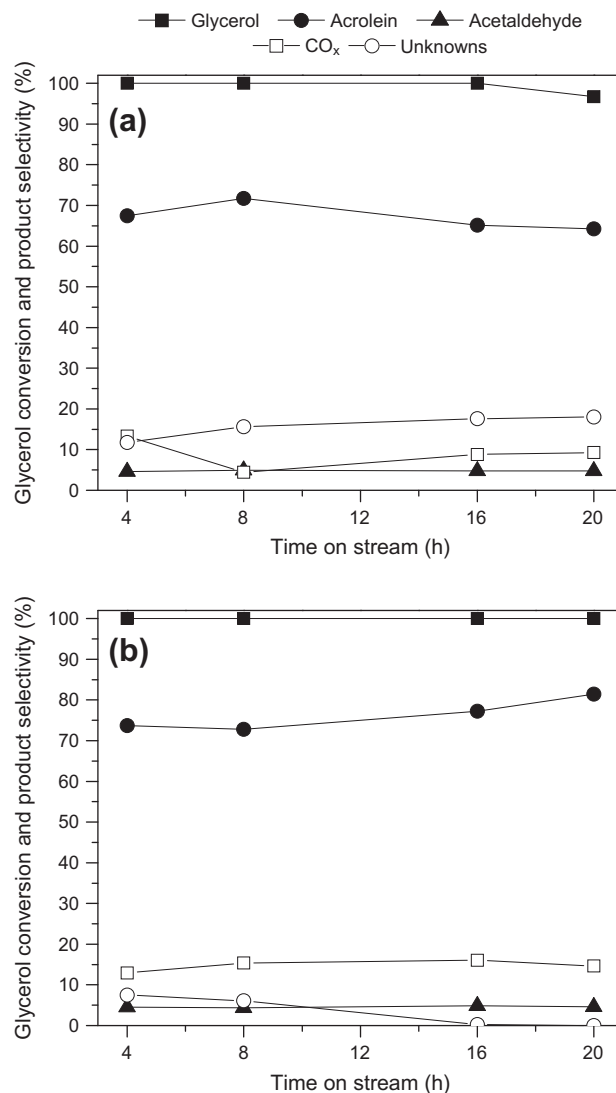


**Fig. 9.** Glycerol conversion (■) and selectivities to acrolein (●), acetaldehyde (▲), CO<sub>x</sub> (□) and unknowns (○) as a function of time on stream (TOS) for (a) 0.5Nb0.5WAl and (b) 1WTi at 305 °C. Amount catalyst: 0.3 g. Feed: 3.6 ml/h 20 wt% aqueous glycerol vaporized in 12 ml/min Ar and 3 ml/min O<sub>2</sub>. Glycerol WHSV: 2.54 h<sup>-1</sup>. Small amounts of propionaldehyde and acetone were also formed.

at 3732 and 3685 cm<sup>-1</sup>, which all are typical of the anatase phase and attributed to Ti–OH groups in different coordination [82,83]. Surface modification with Nb- and W-oxides was observed to lead to the almost complete disappearance of the OH bands of TiO<sub>2</sub>.

The spectrum in Fig. 11 of the Al<sub>2</sub>O<sub>3</sub> support exhibits the typical band pattern of transitional alumina. The two peaks at 3790 (shoulder) and 3770 cm<sup>-1</sup> have been assigned to terminal OHs linked to one tetrahedrally coordinated Al ion in either a non-vacant environment or near a cation vacancy, respectively [84]. A strong band appears at 3723 cm<sup>-1</sup>, which is from terminal OHs bonded to octahedrally coordinated Al ions, and the bands at 3675 and 3570 cm<sup>-1</sup> have been assigned to bridging and residual triply-bridging hydroxyl groups, respectively [84]. Similar to the TiO<sub>2</sub>-supported catalysts, deposition of W- and Nb-oxide on the Al<sub>2</sub>O<sub>3</sub> surface strongly reduce the intensity of the hydroxyl bands as illustrated in Fig. 11 by the spectrum for 0.5Nb0.5WAl, showing that the OH features from Al<sub>2</sub>O<sub>3</sub> have almost completely disappeared and are masked by a broad and weak absorption. Also, deposition of niobia was found to give a similar spectrum.

The spectra of the SiO<sub>2</sub>-supported catalysts, which are exemplified in Fig. 11 by the spectrum for 0.5Nb0.5WSi, show a main band at 3750 cm<sup>-1</sup> due to free silanol groups together with a broad absorption at lower frequencies from OH groups interacting with H-bonds [85]. Although more intense, the spectrum of the pure support has identical spectral features.

### 3.7.2. Pyridine as a probe molecule for acidic sites

Infrared spectra recorded after adsorption of pyridine and subsequent outgassing at 110 °C are displayed in Fig. 12 for the supports and some selected catalysts. The spectrum for the TiO<sub>2</sub> support shows bands at 1605, 1574, 1490, and 1445 cm<sup>-1</sup> from pyridine adsorbed on Lewis acidic Ti ions [86]. On Al<sub>2</sub>O<sub>3</sub>, the adsorption of pyridine gives rise to sharp bands at 1620–1614, 1577, 1492 and 1449 cm<sup>-1</sup> from pyridine interacting with Lewis acidic coordinatively unsaturated Al ions [84]. In case of SiO<sub>2</sub>, only very weak bands appear, originating from adsorbed pyridine interacting with the surface through H-bonds [85].

Deposition of W- and Nb-oxide on the supports generates Brønsted acid sites, which fact is demonstrated by pyridine

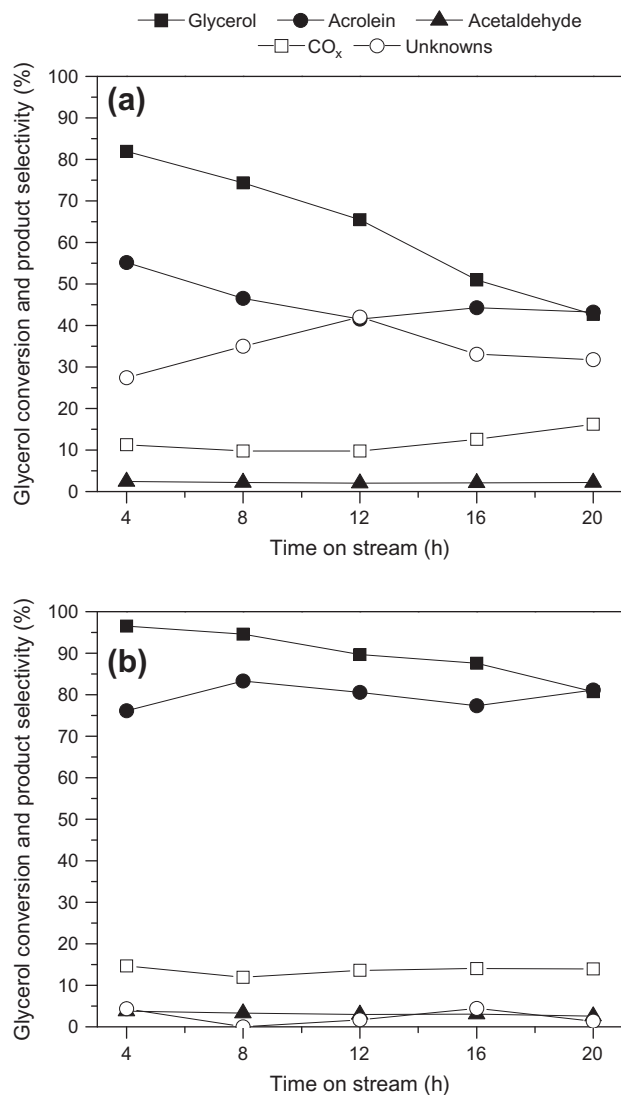


**Fig. 10.** Glycerol conversion (■) and selectivities to acrolein (●), acetaldehyde (▲), CO<sub>x</sub> (□) and unknowns (○) as a function of time on stream (TOS) for (a) 0.5Nb0.5WAl and (b) 1WTi at 305 °C. Amount catalyst: 0.1 g. Feed: 3.6 ml/h 20 wt% aqueous glycerol vaporized in 12 ml/min Ar and 3 ml/min O<sub>2</sub>. Glycerol WHSV: 7.55 h<sup>-1</sup>. Small amounts of propionaldehyde and acetone were also formed.

adsorption giving a typical band at 1540 cm<sup>-1</sup>. That band, which is due to the 19-a ring vibrational mode of the pyridinium ion [87], is clearly seen in the spectra for 0.5Nb0.5WTi and 0.5Nb0.5WAl in Fig. 12. Although very weak, the same band can be distinguished in the spectrum for 0.5Nb0.5WSi together with stronger bands from adsorption at Lewis acidic sites, i.e., coordinatively unsaturated W and Nb ions as well as residual support ions.

The concentrations of Lewis (LAS) and Brønsted (BAS) acidic centers, which are given in Table 5, were calculated from the intensities of the bands at ~1450 and ~1540 cm<sup>-1</sup>, respectively, following the method reported by Emeis [54]. The data show that Al<sub>2</sub>O<sub>3</sub> and TiO<sub>2</sub> have rather similar concentrations of LAS, whereas SiO<sub>2</sub> has no Lewis acidity. For the Al<sub>2</sub>O<sub>3</sub>- and TiO<sub>2</sub>-supported samples, the concentration of LAS varies in a complex manner with the composition. Conversely, on SiO<sub>2</sub>, the deposition of NbO<sub>x</sub> and WO<sub>x</sub> leads to the concentration of LAS increases. Moreover, besides Lewis acidity, the data in Table 5 show that the catalysts with Nb and/or W, opposed to the bare supports, have Brønsted acid sites. For all compositions, the concentration of BAS is higher for the TiO<sub>2</sub>-supported catalysts than for the corresponding Al<sub>2</sub>O<sub>3</sub>-sup-

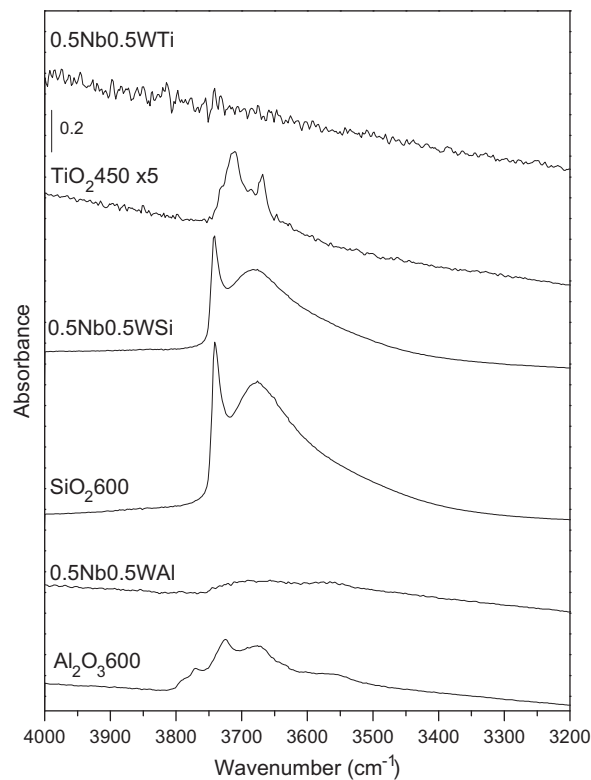


**Fig. 11.** FTIR spectra of the OH stretching region of the pure powder supports and the supported 0.5Nb0.5W catalysts after outgassing for 30 min. The alumina and silica samples were outgassed at 500 °C and the titania samples at 450 °C.

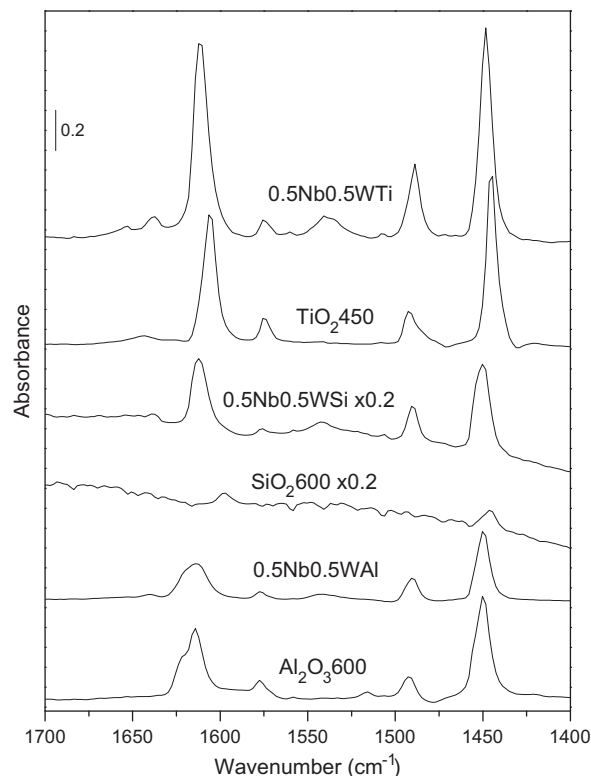


**Fig. 12.** FTIR spectra of the supports and the supported catalysts with Nb/W = 1 recorded after adsorption of pyridine and subsequent outgassing at 110 °C. The figure displays the spectra after subtraction of the spectrum for the heat-treated sample.

**Table 5**  
Acidity of catalysts and supports.

Catalyst	Concentration of LAS <sup>a</sup> ( $\mu\text{mol}/\text{m}^2$ )	Concentration of BAS <sup>b</sup> ( $\mu\text{mol}/\text{m}^2$ )
Al <sub>2</sub> O <sub>3</sub> 600	2.56	0.00
1NbAl	2.69	0.23
1WAl	2.95	0.58
0.25Nb0.75WAl	2.16	0.22
0.5Nb0.5WAl	1.77	0.27
0.75Nb0.25WAl	2.11	0.29
SiO <sub>2</sub> 600	0.00	0.00
1NbSi	0.43	0.14
1WSi	0.35	0.06
0.25Nb0.75WSi	0.41	0.08
0.5Nb0.5WSi	0.50	0.10
0.75Nb0.25WSi	0.65	0.16
TiO <sub>2</sub> 450	2.92	0.00
1NbTi	2.27	0.33
1WTi	1.19	0.60
0.25Nb0.75WTi	1.62	1.01
0.5Nb0.5WTi	4.02	0.75
0.75Nb0.25WTi	2.07	0.53

<sup>a</sup> The concentration of Lewis acidic sites (LAS) as determined from the area of the infrared band at  $\sim 1450\text{ cm}^{-1}$  from adsorbed pyridine by using Emeis' method [54].

<sup>b</sup> The concentration of Brønsted acid sites (BAS) as determined from the area of the infrared band at  $\sim 1540\text{ cm}^{-1}$  from adsorbed pyridine by using Emeis' method [54].

ported samples and is the lowest for the SiO<sub>2</sub>-supported catalysts. Compared with a monolayer loading of NbO<sub>x</sub>, the corresponding loading of WO<sub>x</sub> has higher concentration of BAS when supported on Al<sub>2</sub>O<sub>3</sub> and TiO<sub>2</sub>, but lower concentration on SiO<sub>2</sub>. On Al<sub>2</sub>O<sub>3</sub>, the compositions with both Nb and W have similar concentration of BAS as 1NbAl. For the SiO<sub>2</sub>-supported samples, the concentration of BAS increases with the Nb/W ratio of the sample. A symbiosis effect is observed for the TiO<sub>2</sub>-supported catalysts in that the preparations with both Nb and W have higher concentration of BAS than that of a linear combination of the values for 1WTi and 1NbTi.

### 3.7.3. CO<sub>2</sub> as a probe molecule for basic sites

CO<sub>2</sub> can be used as a spectroscopic probe molecule for basic sites, to which CO<sub>2</sub> is chemisorbed in the form of carbonate and bicarbonate species due to interaction with nucleophilic O<sup>2-</sup> and hydroxyl centers, respectively, whereas the adsorption on non-basic surfaces is almost absent [88–90].

On the Al<sub>2</sub>O<sub>3</sub> support, the adsorption of CO<sub>2</sub> at room temperature yields the spectrum shown in Fig. 13. The main sharp bands at 1652, 1448, and 1228 cm<sup>-1</sup> are due to the vibrational modes of HCO<sub>3</sub><sup>-</sup> species at the surface, while the weaker and broader shoulder components above 1700 cm<sup>-1</sup> and at 1600–1595 and 1477 cm<sup>-1</sup> are assigned to carboxylate and carbonate species in different coordinations [91]. The minor components at 1611, 1579, and 1334 cm<sup>-1</sup> are also from adsorbed carbonate and carboxylate species. Nb- and W-oxide deposition dramatically reduces the intensity of the bicarbonate and carbonate bands, which almost disappear as exemplified by the spectrum in Fig. 13 for 1WAl. Thus, the deposition and interaction of NbO<sub>x</sub> and WO<sub>x</sub> species with the support surface yield by far less basic character to the surface. Moreover, CO<sub>2</sub> on the Al<sub>2</sub>O<sub>3</sub> support gives also a sharp and strong band at 2356 cm<sup>-1</sup>, which is due to the end-on linear form of CO<sub>2</sub> coordinating to a Lewis acidic site through an oxygen lone pair of electrons [92]. Also, that band is slightly asymmetric, pointing to the existence of different types of Lewis acid sites at the alumina surface. In the spectrum in Fig. 13 for 1WAl, the band is clearly split, in which the appearance is a further evidence for the deposition of WO<sub>x</sub> on the surface creating new Lewis acid sites of different strength.

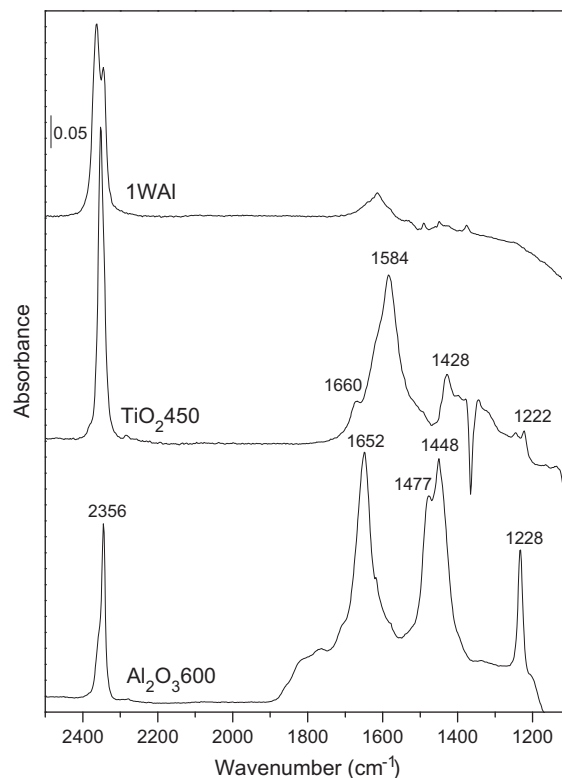


**Fig. 13.** FTIR spectra of calcined TiO<sub>2</sub>, calcined Al<sub>2</sub>O<sub>3</sub>, and the 1WAl catalyst recorded after adsorption of CO<sub>2</sub> at room temperature and subsequent evacuation for 30 min. The spectrum for the pure heat-treated solid and the contribution from gaseous CO<sub>2</sub> have been subtracted.

Concerning the spectrum in Fig. 13 for the TiO<sub>2</sub> support, it shows a band at 1584 cm<sup>-1</sup> from carbonate species and weak bands from bicarbonate species at 1660, 1428, and 1222 cm<sup>-1</sup> [91]. The TiO<sub>2</sub>-supported catalysts with Nb and W showed the same bands, although strongly reduced in intensity, indicating that the deposition of these elements decreases the basic character of the surface. Similar to the Al<sub>2</sub>O<sub>3</sub> support, the TiO<sub>2</sub> support gives a strong band ( $\sim 2360\text{ cm}^{-1}$ ) from molecularly adsorbed CO<sub>2</sub> coordinating to Lewis acidic sites.

No evidence was observed of CO<sub>2</sub> chemisorption on the SiO<sub>2</sub> support and the SiO<sub>2</sub>-supported catalysts, confirming the covalent nature of the Si–O, Nb–O, and W–O bonds.

## 4. Discussion

### 4.1. Nature, structure, and dispersion of the surface species

According to the XPS surface analysis data in Table 3, the dispersion of WO<sub>x</sub> and NbO<sub>x</sub> depends on the type of oxide support. As indicated by the support metal contents, the coverage of the support generally decreases in the order TiO<sub>2</sub> > Al<sub>2</sub>O<sub>3</sub> > SiO<sub>2</sub>. This trend is also confirmed by the XRD patterns of the freshly prepared catalysts in Figs. 1–3. In fact, as exemplified in Fig. 3, the samples supported on TiO<sub>2</sub> show the presence of neither crystalline Nb<sub>2</sub>O<sub>5</sub> nor WO<sub>3</sub>. The good dispersion on TiO<sub>2</sub> is also supported by the fact that the surface of titania appears to be highly dehydroxylated after metal oxide deposition, as exemplified by the spectrum for 0.5Nb0.5WTi in Fig. 11. Moreover, in agreement with previous observations for WO<sub>x</sub>/TiO<sub>2</sub> [93,94], the data in Table 1 on the surface areas in m<sup>2</sup>/g support show that the deposition of W- and Nb-oxide on the TiO<sub>2</sub> surface reduces the tendency during calcination toward sintering compared to the pure support, an

observation that is an indirect support for the dispersion of the active species being good on titania. On alumina, monoclinic  $\text{WO}_3$  is detected by XRD only at the highest W loading, whereas no crystalline  $\text{Nb}_2\text{O}_5$  polymorph is detected even at high Nb-loadings (see Fig. 1). Also, the  $\text{Al}_2\text{O}_3$  surface seems to be almost completely dehydroxylated after metal oxide deposition as emphasized in Fig. 11. However, the XPS data in Table 3 for the 1W- and 1Nb-samples indicate that  $\text{NbO}_x$  and  $\text{WO}_x$  are slightly less dispersed on  $\text{Al}_2\text{O}_3$  than on  $\text{TiO}_2$ , whereas rather the opposite trend is noticed for the mixed samples. Regarding the preparations on  $\text{Al}_2\text{O}_3$ , the XRDs in Fig. 1 possibly indicate the formation of some  $\text{WO}_{2.92}$  in the mixed Nb–W-oxide samples.  $\text{WO}_{2.92}$  or  $\text{W}_{25}\text{O}_{73}$  is a structure with crystallographic shear planes and tungsten in octahedral coordination [95]. The presence of tungsten in a reduced oxidation state in our catalysts can be ruled out, because the samples have been calcined in air at relatively high temperature (600 °C). Therefore, considering that the ionic radii of  $\text{W}^{6+}$  and  $\text{Nb}^{5+}$  in octahedral coordination are 0.74 and 0.78 Å, respectively, it can be suggested that the  $\text{WO}_{2.92}$  phase in the catalysts has some Nb substituted for W, giving the composition  $\text{W}(\text{VI})_{0.84}\text{Nb}(\text{V})_{0.16}\text{O}_{2.92}$ . For the preparations on  $\text{SiO}_2$ , the XRDs in Fig. 2 show extensive formation of monoclinic  $\text{WO}_3$  and orthorhombic  $\text{Nb}_2\text{O}_5$  in agreement with the XPS results in Table 3, showing for Nb- and W-oxide lower degree of dispersion on  $\text{SiO}_2$  than on  $\text{TiO}_2$  and  $\text{Al}_2\text{O}_3$ . These results agree with the infrared spectra of the OH region in Fig. 11, displaying identical spectral features for calcined  $\text{SiO}_2$  and the 0.5Nb0.5WSi catalyst, although somewhat less intense for the latter. The small difference in intensity indicates that only a part of the silanol groups has been involved in grafting of surface oxide species.

In agreement with the XRD and XPS results, showing that niobia and tungsten oxide are effectively dispersed over the  $\text{Al}_2\text{O}_3$  and  $\text{TiO}_2$  surfaces, are the results on  $\text{CO}_2$  adsorption. These data show that the bands from carbonate and bicarbonate species on the bare  $\text{Al}_2\text{O}_3$  and  $\text{TiO}_2$  surfaces are almost absent after deposition of monolayer loadings of Nb- and W-oxides at the surfaces (see Section 3.7.3. and Fig. 13). This observation indicates that nucleophilic oxide and hydroxide species at the surface are involved in the bonding to Nb- and W-oxide species, thus losing their basicity. A direct evidence for the existence of surface  $\text{WO}_x$  and  $\text{NbO}_x$  species on  $\text{Al}_2\text{O}_3$  and  $\text{TiO}_2$  interacting with the support are the Raman spectra in Figs. 4 and 6, respectively, showing bands from hydrated polytungstate ( $970\text{--}980\text{ cm}^{-1}$ ) [56,62,70,71] and hydrated niobia ( $910\text{ cm}^{-1}$ ) [66,68,69] surface species. Although the XRDs in Fig. 2 and the XPS quantifications in Table 3 confirm extensive formation of bulk  $\text{WO}_3$  and  $\text{Nb}_2\text{O}_5$  phases on  $\text{SiO}_2$ , the Raman spectra in Fig. 5 show some formation of hydrated polytungstate species ( $957\text{ cm}^{-1}$ ). Additionally, in the spectra for 1NbSi and the  $\text{NbWO}_x/\text{SiO}_2$  samples, there is a band showing a continuous shift from  $720\text{ cm}^{-1}$  to  $760\text{ cm}^{-1}$  with decreasing Nb-content from 1NbSi to 0.25Nb0.75WSi. Moreover, the band is most intense for the composition for 0.5Nb0.5WSi. Consulting the literature on silica-supported niobia [96,97], no clear assignment of the band can be made. As the band is complex and the intensity is dependent on the W-content of the sample, the band can be proposed to originate from niobia surface species interacting with adjacent  $\text{WO}_x$  moieties in different configurations.

Comparing with reference compounds, the pre-edge features of the Nb K- and W  $L_1$ -edge XANES spectra in Fig. 7 indicate that both Nb and W on the catalysts are in distorted octahedral environments. However, since the spectra give the average coordination of the atoms, it cannot be excluded that the additional coordination can prevail. In particular, the spectra for 1WAl and 1WTi show a slightly more distinct pre-peak compared to 1WSi and the  $\text{WO}_3$  reference, indicating the possible presence of some  $\text{WO}_4$  tetrahedral and  $\text{WO}_5$  square pyramidal units in addition to the hydrated octahedral units [79,80,98]. Both the main-edge position in XANES

and the XPS data in Table 2 clearly agree with Nb and W being in their highest oxidation states.

The total loading of W- and Nb-oxide on the supported catalysts was  $11.6\text{ }\mu\text{mol/m}^2$  surface area of support, corresponding to  $7.0\text{ atoms/nm}^2$  (Table S1). In case of titania, we found the formation of neither  $\text{WO}_3$  nor  $\text{Nb}_2\text{O}_5$ , indicating complete dispersion on the support. Our finding here is in agreement with the values given in the literature on the monolayer capacities for  $\text{WO}_x/\text{TiO}_2$  and  $\text{NbO}_x/\text{TiO}_2$ , which have been reported to be in the range  $4.1\text{--}7.5\text{ W atoms/nm}^2$  [71,94,99,100] and  $6.8\text{ Nb atoms/nm}^2$  [69], respectively. For the  $\text{Al}_2\text{O}_3$ -supported samples, the XRDs in Fig. 1 show some formation of crystalline  $\text{WO}_3$  in 1WAl, whereas for 1NbAl, there are no peaks from crystalline niobia. This difference between the elements agrees with previous findings that the monolayer capacities on  $\text{Al}_2\text{O}_3$  are 5.9 and 5 atoms/ $\text{nm}^2$  for niobia [69] and tungsten oxide [101], respectively. For the silica-supported catalysts, the XRDs in Fig. 2 and the XPS data in Table 3 show that the dispersion of niobia and tungsten oxide is low on this support, which is in correspondence with the monolayer capacities being reported to be about  $0.5\text{ atoms/nm}^2$  for both tungsten oxide [56] and niobia [69] on silica.

Our results showing that the dispersion and the monolayer capacity for niobia and tungsten oxide differ on the three supports can be explained on the basis of the isoelectric point of the support, the pH of the aqueous solution containing the salt of the active metal, and the charge of the ion to be adsorbed [102]. The supports in the present study  $\theta\text{-Al}_2\text{O}_3$ ,  $\text{SiO}_2$ , and  $\text{TiO}_2$ -anatase have isoelectric points of about 8, 2 and 6, respectively [103], and the aqueous solutions being used for impregnation of the supports with dissolved W and/or Nb salts were measured to be slightly acidic (pH  $\sim 4\text{--}5$ ). Thus, one can expect in these solutions that the surfaces of  $\text{Al}_2\text{O}_3$  and  $\text{TiO}_2$  are positively charged, whereas the  $\text{SiO}_2$  surface is negatively charged. In acidic aqueous solutions, the tungsten [104] and niobium [105] species are in the form of polyoxo anions. Thus, it can be expected that the  $\text{Al}_2\text{O}_3$  and  $\text{TiO}_2$  surfaces interact far better than the  $\text{SiO}_2$  surface with the anionic W- and Nb-species, resulting in better dispersion and coverage on the former two supports. Besides the electrostatic effects in solution, also the nature of the OH surface groups of the oxide support has to be considered. In fact, OH groups may act as anchoring sites for active metal oxide species during the impregnation procedure. In this context, the behavior of  $\text{Al}_2\text{O}_3$  and  $\text{TiO}_2$  is quite different from that of  $\text{SiO}_2$ . Due to the highly ionic character of the first two supports [106], the OH groups here are located in close proximity to Lewis acid cations and active  $\text{O}^{2-}$  anions. These structures may act synergistically as grafting sites for surface oxide species. In this regard, the behavior of  $\text{SiO}_2$  is different due to its covalent character, which gives rise to mostly isolated or few clustered silanol groups on an essentially inert surface, resulting in poor dispersion of the supported oxide phases.

#### 4.2. Catalytic performance and role of acidity

Of the investigated catalysts, the  $\text{Al}_2\text{O}_3$ -supported ones are generally the best (Table 4), where the samples with tungsten give selectivities and yields to acrolein of about 67–72% at high glycerol conversion. For these samples, the carbon balance is around 80–90%. The corresponding compositions supported on  $\text{TiO}_2$  generally are the second best, giving selectivities and yields to acrolein in the range 55–66%. Irrespective of the support, all samples with monolayer loading of niobia show similar selectivity to acrolein (55–60%). Our catalytic results are in general agreement with previously reported data for similar systems, of which there are only a few studies in the literature. Shiju et al. [45] studied the effect of loading and calcination temperature on the catalytic performance of silica-supported niobia catalysts and report a selectivity to

acrolein of ~65% at high conversion of glycerol. In another study, Ulgen and Hoelderich [40] screened different types of titania as catalyst support for  $\text{WO}_3$  in glycerol dehydration. Under anaerobic conditions, the samples gave selectivities to acrolein around 75% at glycerol conversions in the range 76–89%. To the best of our knowledge, so far no studies have been reported dealing with  $\text{Al}_2\text{O}_3$ -supported Nb- and W-oxides for glycerol dehydration to produce acrolein. In a previous study, we used monoclinic  $\text{ZrO}_2$  as a support for niobia and tungsten oxide [41]. Compared with the present  $\text{Al}_2\text{O}_3$ - and  $\text{TiO}_2$ -supported samples, the corresponding compositions on monoclinic  $\text{ZrO}_2$  in most cases show slightly better performance with selectivities and yields to acrolein close to 75% and a carbon balance in the range 85–90%.

As can be seen in Table 4, all catalysts that were screened for glycerol dehydration exhibit nearly full conversion apart from  $\text{SiO}_2/600$ ,  $1\text{WSi}$ , and  $1\text{NbSi}$ . In particular,  $\text{SiO}_2$  shows almost no activity yielding mainly  $\text{CO}_x$ . According to the XPS data in Table 3,  $1\text{WSi}$  and  $1\text{NbSi}$  exhibit the lowest dispersion of active metal among the supported catalysts, explaining their reduced activity. In previous studies [24,33,41,107–109], a dependence of the catalytic activity on the total number of acidic sites has been pointed out. In this respect, our data in Tables 4 and 5 give no clear support. Although the total concentration of acidic sites (LAS + BAS) is the lowest for silica and the silica-supported samples, the data in Table 5 show no significant difference between the less active  $1\text{NbSi}$  and  $1\text{WSi}$  and the more active  $\text{NbWO}_x/\text{SiO}_2$  samples. Obviously, besides acidity, also structure and interaction of niobia and tungsten oxide with the support are important.

All the supported catalysts give acrolein as a main reaction product, whose selectivity depends on the type of support (Table 4). In the literature, there is general agreement that Brønsted acid sites (BAS) are involved in the reaction pathway leading to acrolein formation from glycerol on acidic catalysts [16,25,30,37,41,43,46,109,110]. In Fig. 14, the acrolein selectivities for the supported catalysts and the silica support are plotted against the concentration of Brønsted acid sites (Table 5). Clearly, the sigmoidal trend indicates that the selectivity to acrolein increases with the increasing amount of BAS until leveling off. It is worth emphasizing that the values for the calcined alumina and titania supports are not included in Fig. 14. In fact, in agreement with previous reports [27,28], these supports show appreciable selectivity to acrolein (Table 4) even without exhibiting any Brønsted acidity (Table 5 and Fig. 12). This observation can be explained by a certain amount of the Lewis acid sites (LAS) on these supports (Table 5) being converted into BASs at the reaction conditions by interacting with the steam present in the system [25,35].

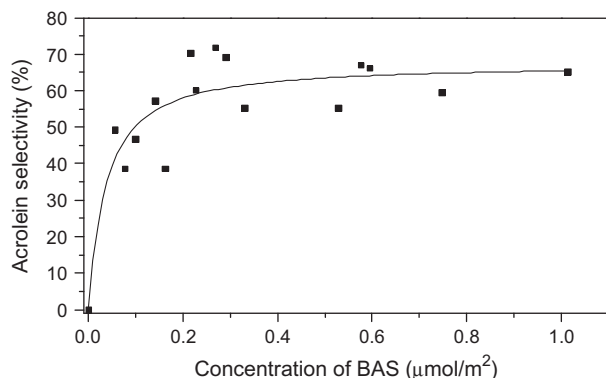


**Fig. 14.** Plot of the selectivity to acrolein vs. the concentration of Brønsted acid sites for the  $\text{Al}_2\text{O}_3$ -,  $\text{SiO}_2$ -, and  $\text{TiO}_2$ -supported catalysts and the  $\text{SiO}_2$  support. The values plotted are from Tables 4 and 5 but do not include the data for the  $\text{Al}_2\text{O}_3$  and  $\text{TiO}_2$  supports as explained in Section 4.2.

Under anaerobic conditions, the major by-product detected over the  $\text{Al}_2\text{O}_3$ - and  $\text{SiO}_2$ -supported catalysts is hydroxyacetone with selectivities in the range 8–18% and 4–8%, respectively (Table 4). Over the  $\text{TiO}_2$ -supported catalysts, on the contrary, only traces of hydroxyacetone are formed. Several works suggest that the undesired conversion of glycerol into hydroxyacetone occurs over basic sites [39,40,46,107,111,112]. This assumption, however, is in disagreement with our results since hydroxyacetone is detected over all  $\text{Al}_2\text{O}_3$ - and  $\text{SiO}_2$ -supported catalysts as the data in Table 4 show. Among these samples, only  $\text{Al}_2\text{O}_3/600$  and  $\text{TiO}_2/450$  exhibit basic sites, as exemplified in Fig. 13 (see Section 3.7.3.). Hence, we have reasons to believe that the monodehydration of glycerol leading to the formation of hydroxyacetone is catalyzed by Lewis acid sites, as has been proposed in earlier investigations [25,113]. In fact, as shown in Fig. 15, the selectivity to hydroxyacetone correlates quite well with the concentration of LAS, although some values are slightly scattered. Also, the same correlation is true for the corresponding yield, considering that the selectivity values in Table 4 are for the almost complete conversion of glycerol. It is worth mentioning that the values for the  $\text{TiO}_2$ -supported catalysts are not included in Fig. 15. The reason is that these samples, although exhibiting appreciable concentrations of LAS (Table 5), they give very low selectivities to hydroxyacetone (Table 4). This seemingly anomalous behavior can be related to the by-product distribution being different on the various supports. The data in Table 4 show that the  $\text{TiO}_2$ -supported samples, compared with the  $\text{Al}_2\text{O}_3$ - and  $\text{SiO}_2$ -supported samples, give more propionaldehyde, acetone, CO and in a few cases acetaldehyde. Apparently, the difference in product distribution suggests that the niobia and tungsten oxide species on titania are more active than the corresponding species on  $\text{Al}_2\text{O}_3$  and  $\text{SiO}_2$  for the further transformation of hydroxyacetone to acetone and CO. In fact, it has been demonstrated that hydroxyacetone may produce not only acetone and CO but also acetaldehyde, propionaldehyde, and acetic acid [46]. In the present study, however, we did not detect any formation of acetic acid. Thus, our results infer that  $\text{TiO}_2$ , compared with  $\text{Al}_2\text{O}_3$  and  $\text{SiO}_2$ , give enhanced redox capability to supported tungsten and niobium oxide species. In fact, it has been observed in TPR experiments that supported  $\text{WO}_x$  is reduced at lower temperature on  $\text{TiO}_2$  (>380 °C) [114] than on  $\text{Al}_2\text{O}_3$  (>600 °C) [115] and  $\text{SiO}_2$  (>630 °C) [116].

#### 4.3. Catalyst deactivation

It is well known that deactivation of the catalyst takes place in glycerol dehydration over essentially all types of catalysts [1,2,16–18,20–26,28,30–32,34,37–41,43–50,108,109,117], which is in

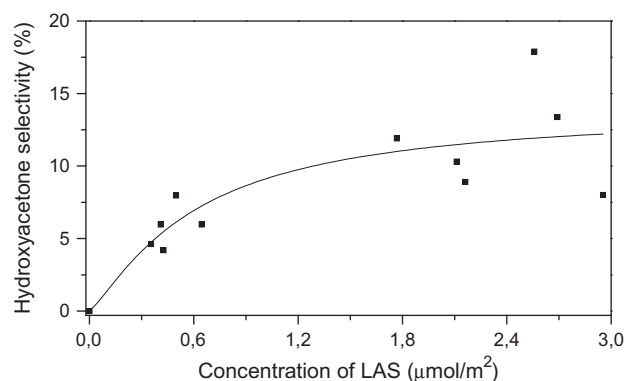


**Fig. 15.** Plot of the selectivity to hydroxyacetone vs. the concentration of Lewis acid sites for the  $\text{Al}_2\text{O}_3$ - and  $\text{SiO}_2$ -supported catalysts. The values are from Tables 4 and 5.

agreement with the present results in Figs. 8–10. In the literature, the deactivation has been ascribed to the adsorption of heavy compounds and the formation of coke at the catalyst surface [2,14,17,20,21,27,28,41,43,44]. Elemental analysis of the deposit formed on niobia gave the H/C ratio 0.50–0.53 [43], and dissolution in dimethyl sulfoxide of the deposit from a vanadium phosphate catalyst gave mass fragments in the range 200–500 amu on a mass spectrometer [50]. These results confirm that a substantial amount of the deposit is in the form of carbonaceous species. In the present study, the formation of deactivating species is further confirmed by the change in the pore properties for all the catalysts, as shown in Table 1 comparing the data for freshly prepared with used samples. Another support is the fact that the carbon balances listed in Table 4 are incomplete. In particular, for the bare  $\text{Al}_2\text{O}_3$  and  $\text{TiO}_2$  supports, the poor mass balances may to some extent be attributed to the formation of condensation products. As shown in Fig. 13, the  $\text{Al}_2\text{O}_3$  and  $\text{TiO}_2$  supports exhibit basic sites, which may catalyze the formation of polyglycerols [24,44,118] and other high-boiling compounds responsible for deactivation [119]. The improved carbon balance for the  $\text{Al}_2\text{O}_3$ - and  $\text{TiO}_2$ -supported catalysts may be ascribed to the suppression of basic sites, as exemplified in Fig. 13 (see Section 3.7.3.), and to the formation of Brønsted acid sites (Table 5 and Fig. 12), being selective for acrolein formation (Fig. 14). For these catalysts, and also the  $\text{SiO}_2$ -supported ones, it is reasonable to assume that the missing carbon belongs to compounds, which may derive from side-reactions of acrolein [25,27,37]. However, a contribution from consecutive reactions of other products, such as hydroxyacetone, cannot be ruled out [19,25,32].

The deactivation behaviors for 0.5Nb0.5WAl and 1WTi under anaerobic conditions are depicted in Fig. 8. These catalysts were selected for stability testing since they according to the data in Table 4 gave the best performance to acrolein among the  $\text{Al}_2\text{O}_3$ - and  $\text{TiO}_2$ -supported catalysts, respectively. Comparing the data in Table 1 for the supported catalysts before and after use in glycerol dehydration, it is seen for the preparations on  $\text{Al}_2\text{O}_3$  that the surface area, the pore size, and the pore volume all show a relatively modest decrease. For the  $\text{TiO}_2$ -supported catalysts, on the other hand, the data show that both the surface area and the pore volume have decreased considerably, whereas the pore size has increased somewhat. The different behaviors of the catalysts on the two supports indicate two different types of deactivation. For the  $\text{Al}_2\text{O}_3$ -supported samples, the changes in textural properties including the decreasing pore size imply that heavy compounds and coke molecules are deposited on the pore walls (site blocking). On the contrary, the changes occurring for the titania-supported samples showing some increase in the measured pore size is a clear signal that smaller pores are totally blocked (pore blocking). The corresponding changes for the  $\text{SiO}_2$ -supported catalysts suggest that deactivation occurs by both mechanisms.

The performances of 0.5Nb0.5WAl and 1WTi with time on stream under aerobic conditions are displayed in Figs. 9 and 10. Except for the oxygen pressure, the data in Fig. 9 are for the same reaction conditions and space velocity ( $\text{WHSV} = 2.54 \text{ h}^{-1}$ ) as the corresponding data in Fig. 8 for anaerobic conditions. A comparison of the time on stream behaviors clearly reveals that the catalysts are more stable when co-feeding oxygen with glycerol. Moreover, the selectivity to acrolein over 0.5Nb0.5WAl is slightly lower ~68% under aerobic conditions compared to the value ~74% for anaerobic conditions, whereas 1WTi shows an opposite behavior. In the absence of oxygen, the selectivity decreases during use in the reaction (20 h) from 72% to 55%, whereas under aerobic conditions, the selectivity and the yield to acrolein increase up to 80%. Also, in our previous study of zirconia-supported  $\text{NbO}_x$  and  $\text{WO}_x$ , we observed that oxygen addition gives improved stability to the catalyst; however, in that case, oxygen did not affect much the selectivity to acrolein [41]. Opposed to the present results, in a

previous study of  $\text{WO}_3$  on  $\text{TiO}_2$ , addition of oxygen was observed to give a minor decrease in the selectivity to acrolein [40], whereas the opposite effect was observed for  $\text{WO}_3$  on  $\text{ZrO}_2$  [39]. The reason for the catalyst being more stable in the presence of oxygen is that oxygen improves the regeneration of active sites by reacting with coke precursors and heavy compounds to give  $\text{CO}_x$  [41]. In fact, comparing Figs. 8 and 9, it is seen that an oxidative atmosphere produces more  $\text{CO}_x$  and reduces the formation of heavy compounds. The latter species possibly account for most of the unidentified products.

To judge the stability of the catalysts under aerobic conditions, the data in Fig. 9 cannot be used since they are for almost full conversion (low space velocity). In this regard, the performances in Fig. 10 for a higher space velocity are more appropriate. Here, we can see that some deactivation of the catalysts occurs also under aerobic conditions. The stability of the two catalysts 0.5Nb0.5WAl and 1WTi under anaerobic and aerobic conditions cannot be compared simply by considering the conversion changes in Figs. 8 and 10, respectively, since the data are for different space velocities and conversion levels. Therefore, rate constants were calculated assuming a first order rate dependence on glycerol since water is present in excess, which also gives approximately equimolar conditions. The ratio  $k_{20}/k_4$  between the rate constant after 20 h reaction ( $k_{20}$ ) and the corresponding constant for 4 h reaction ( $k_4$ ) is 0.135 and 0.0176 for 0.5Nb0.5WAl and 1WTi, respectively, as calculated from the data in Fig. 8a and b, respectively. For aerobic conditions, the data in Fig. 10 give the  $k_{20}/k_4$  ratios 0.328 and 0.485 for 0.5Nb0.5WAl and 1WTi, respectively. Thus, comparing the  $k_{20}/k_4$  ratios and the catalytic performances in Figs. 8–10 shows in the absence of oxygen that 0.5Nb0.5WAl is both the most stable and the best performing catalyst with selectivity to acrolein of about 74%. Conversely, under aerobic conditions, 1WTi is the most stable and best performing catalyst giving selectivity to acrolein in the range 75–80%. The better stability in the presence of oxygen of 1WTi (Fig. 10b) compared to 0.5Nb0.5WAl (Fig. 10a) agrees with the amount of unidentified products including coke and coke precursors being the lowest over the former catalyst, giving improved selectivity to acrolein.

## 5. Conclusions

Catalysts with theoretical monolayer loadings of niobium and tungsten oxides on  $\text{Al}_2\text{O}_3$  and  $\text{TiO}_2$  are active and selective for the dehydration of glycerol to form acrolein, whereas the corresponding  $\text{SiO}_2$ -supported compositions are less selective.

The  $\text{Al}_2\text{O}_3$  and  $\text{TiO}_2$  catalyst surfaces exhibit dispersed niobate and tungstate structures. Conversely, predominantly crystalline bulk  $\text{WO}_3$  and  $\text{Nb}_2\text{O}_5$  phases form on the  $\text{SiO}_2$  surface.

All catalysts deactivate with time on stream. However, the deactivation process is considerably reduced when adding oxygen to the feed, mainly because the formation of coke precursors and heavy compounds is reduced.

The selectivities to acrolein and hydroxyacetone correlate with the presence of Brønsted and Lewis acidic sites, respectively.

Under anaerobic conditions, an  $\text{Al}_2\text{O}_3$ -supported catalyst with equimolar amounts of niobia and tungsten oxide is the best performing with a selectivity to acrolein above 70% at full conversion of glycerol. When there is oxygen in the feed, a  $\text{TiO}_2$ -supported tungsten oxide shows excellent performance, giving a selectivity to acrolein around 80% at high glycerol conversion.

## Acknowledgments

The Swedish Research Council (VR) is acknowledged for financial support. Part of the research was carried out at beamline

I811, MAX-lab synchrotron radiation source, Lund University, Sweden. Funding for the beamline I811 project was kindly provided by The Swedish Research Council and The Knut and Alice Wallenberg Foundation.

## Appendix A. Supplementary material

Supplementary data associated with this article can be found, in the online version, at <http://dx.doi.org/10.1016/j.jcat.2013.07.022>.

## References

- [1] A. Martin, U. Armbruster, H. Atia, *Eur. J. Lipid Sci. Technol.* 114 (2012) 10–23.
- [2] B. Katryniok, S. Paul, M. Capron, F. Dumeignil, *ChemSusChem* 2 (2009) 719–730.
- [3] G.W. Huber, S. Iborra, A. Corma, *Chem. Rev.* 106 (2006) 4044–4098.
- [4] [http://www.biodiesel.com/index.php/biodiesel/what\\_is\\_biodiesel](http://www.biodiesel.com/index.php/biodiesel/what_is_biodiesel).
- [5] A. Demirbas, *Biodiesel: A Realistic Fuel Alternative for Diesel Engines*, Springer, London, 2008.
- [6] <http://www.biofuelstp.eu/fuelproduction.html>.
- [7] D.T. Johnson, K.A. Taconi, *Environ. Prog.* 26 (2007) 338–348.
- [8] C.-H. Wong, C.-C. Huang, W.-M. Chen, J.-S. Chang, *Biochem. Eng. J.* 58–59 (2011) 177–183.
- [9] Y. Zheng, X. Chen, Y. Shen, *Chem. Rev.* 108 (2008) 5253–5277.
- [10] C.-H. Zhou, J.N. Beltrami, Y.-X. Fan, G.Q. Lu, *Chem. Soc. Rev.* 37 (2008) 527–549.
- [11] M.O. Guerrero-Peréz, J.M. Rosas, J. Bedia, J. Rodríguez-Mirasol, T. Cordero, *Recent Pat. Chem. Eng.* 2 (2009) 11–21.
- [12] M. Pagliaro, R. Ciriminna, H. Kimura, M. Rossi, C. Della Pina, *Angew. Chem. Int. Ed.* 46 (2007) 4434–4440.
- [13] D. Arntz, A. Fischer, M. Höpp, S. Jacobi, J. Sauer, T. Ohara, T. Sato, N. Shimizu, H. Schwind, *Acrolein and Methacrolein*, Ullmann's Encyclopedia of Industrial Chemistry, Wiley-VCH, 2007, pp. 329–346.
- [14] L. Liu, X.P. Ye, J.J. Bozell, *ChemSusChem* 5 (2012) 1162–1180.
- [15] T. Ohara, T. Sato, N. Shimizu, G. Prescher, H. Schwind, O. Weiberg, K. Marten, H. Greim, *Acrylic Acid and Derivatives*, Ullmann's Encyclopedia of Industrial Chemistry, Wiley-VCH, 2011, pp. 1–18.
- [16] C.-J. Jia, Y. Liu, W. Schmidt, A.-H. Lu, F. Schueth, *J. Catal.* 269 (2010) 71–79.
- [17] Y.T. Kim, K.-D. Jung, E.D. Park, *Appl. Catal. A* 393 (2011) 275–287.
- [18] Y.T. Kim, K.-D. Jung, E.D. Park, *Microporous Mesoporous Mater.* 131 (2010) 28–36.
- [19] A. Corma, G.W. Huber, L. Sauvinauda, P. O'Connor, *J. Catal.* 257 (2008) 163–171.
- [20] A. Witsuthammakul, T. Sooknoi, *Appl. Catal. A* 413 (2012) 109–116.
- [21] Y. Gu, N. Cui, Q. Yu, C. Li, Q. Cui, *Appl. Catal. A* 429–430 (2012) 9–16.
- [22] S.-H. Chai, H.-P. Wang, Y. Liang, B.-Q. Xu, *Appl. Catal. A* 353 (2009) 213–222.
- [23] S.-H. Chai, H.-P. Wang, Y. Liang, B.-Q. Xu, *Green Chem.* 10 (2008) 1087–1093.
- [24] Y.T. Kim, K.-D. Jung, E.D. Park, *Bull. Korean Chem. Soc.* 31 (2010) 3283–3290.
- [25] A. Alhanash, E.F. Kozhevnikova, I.V. Kozhevnikov, *Appl. Catal. A* 378 (2010) 11–18.
- [26] H. Atia, U. Armbruster, A. Martin, *J. Catal.* 258 (2008) 71–82.
- [27] S.-H. Chai, H.-P. Wang, Y. Liang, B.-Q. Xu, *Green Chem.* 9 (2007) 1130–1136.
- [28] E. Tsukuda, S. Sato, R. Takahashi, T. Sodesawa, *Catal. Commun.* 8 (2007) 1349–1353.
- [29] L. Ning, Y. Ding, W. Chen, L. Gong, R. Lin, L. Yuan, Q. Xin, *Chin. J. Catal.* 29 (2008) 212–214.
- [30] Y.T. Kim, S.J. You, K.-D. Jung, E.D. Park, *Bull. Korean Chem. Soc.* 33 (2012) 2369–2377.
- [31] M.H. Haider, N.F. Dummer, D. Zhang, P. Miedziak, T.E. Davies, S.H. Taylor, D.J. Willock, D.W. Knight, D. Chadwick, G.J. Hutchings, *J. Catal.* 286 (2012) 206–213.
- [32] W. Suprun, M. Lutecki, T. Haber, H. Papp, *J. Mol. Catal. A* 309 (2009) 71–78.
- [33] W. Suprun, M. Lutecki, H. Papp, *Chem. Eng. Technol.* 34 (2011) 134–139.
- [34] Q. Liu, Z. Zhang, Y. Du, J. Li, X. Yang, *Catal. Lett.* 127 (2009) 419–428.
- [35] F. Wang, J.-L. Dubois, W. Ueda, *Appl. Catal. A* 376 (2010) 25–32.
- [36] G.S. Patience, Y. Farrie, J.F. Devaux, J.L. Dubois, *Chem. Eng. Technol.* 35 (2012) 1699–1706.
- [37] J.P. Lourenco, M.I. Macedo, A. Fernandes, *Catal. Commun.* 19 (2012) 105–109.
- [38] P. Lauriol-Garbey, S. Loridant, V. Belliere-Baca, P. Rey, J.-M.M. Millet, *Catal. Commun.* 16 (2011) 170–174.
- [39] A. Ulgen, W. Hoelderich, *Catal. Lett.* 131 (2009) 122–128.
- [40] A. Ulgen, W.F. Hoelderich, *Appl. Catal. A* 400 (2011) 34–38.
- [41] M. Massa, A. Andersson, E. Finocchio, G. Busca, F. Lenrick, L.R. Wallenberg, *J. Catal.* 297 (2013) 93–109.
- [42] M. Akizuki, Y. Oshima, *Ind. Eng. Chem. Res.* 51 (2012) 12253–12257.
- [43] S.-H. Chai, H.-P. Wang, Y. Liang, B.-Q. Xu, *J. Catal.* 250 (2007) 342–349.
- [44] P. Lauriol-Garbey, J.M.M. Millet, S. Loridant, V. Belliere-Baca, P. Rey, *J. Catal.* 280 (2011) 68–76.
- [45] N.R. Shiju, D.R. Brown, K. Wilson, G. Rothenberg, *Top. Catal.* 53 (2010) 1217–1223.
- [46] P. Lauriol-Garbey, G. Postole, S. Loridant, A. Auroux, V. Belliere-Baca, P. Rey, J.M.M. Millet, *Appl. Catal. B* 106 (2011) 94–102.
- [47] B. Katryniok, S. Paul, M. Capron, V. Belliere-Baca, P. Rey, F. Dumeignil, *ChemSusChem* 5 (2012) 1298–1306.
- [48] F. Cavani, S. Guidetti, L. Marinelli, M. Piccinini, E. Ghedini, M. Signoretto, *Appl. Catal. B* 100 (2010) 197–204.
- [49] F. Cavani, S. Guidetti, C. Trevisanut, E. Ghedini, M. Signoretto, *Appl. Catal. A* 409–410 (2011) 267–278.
- [50] F. Wang, J.-L. Dubois, W. Ueda, *J. Catal.* 268 (2009) 260–267.
- [51] J.-L. Dubois, C. Duquenne, W. Hölderich, *Process for dehydrating glycerol to acrolein*, International Patent WO 2006/087083, Arkema France, 2006.
- [52] J. Papachryssanthou, E. Bordes, A. Vejux, P. Courtine, R. Marchand, M. Tournoux, *Catal. Today* 1 (1987) 219–227.
- [53] M. Sanati, A. Andersson, *J. Mol. Catal.* 59 (1990) 233–255.
- [54] C.A. Emeis, *J. Catal.* 141 (1993) 347–354.
- [55] JCPDS International Centre for Diffraction Data, *Powder Diffraction File*, Swarthmore, PA, 2010.
- [56] E.I. Ross-Medgaarden, I.E. Wachs, *J. Phys. Chem. C* 111 (2007) 15089–15099.
- [57] R. Moraes, K. Thomas, S. Thomas, S. Van Donk, G. Grasso, J.-P. Gilson, M. Houalla, *J. Catal.* 286 (2012) 62–77.
- [58] M.R.N. Soares, S. Leite, C. Nico, M. Peres, A.J.S. Fernandes, M.P.F. Graca, M. Matos, R. Monteiro, T. Monteiro, F.M. Costa, *J. Eur. Ceram. Soc.* 31 (2011) 501–506.
- [59] A. Spamer, T.I. Dube, D.J. Moodley, C. van Schalkwyk, J.M. Botha, *Appl. Catal. A* 255 (2003) 153–167.
- [60] Y. Wang, Q. Chen, W. Yang, Z. Xie, W. Xu, D. Huang, *Appl. Catal. A* 250 (2003) 25–37.
- [61] S. Chaemchuen, S. Phatanasri, F. Verpoort, N. Sae-ma, K. Suriye, *Kinet. Catal.* 53 (2012) 247–252.
- [62] D. Kim, M. Ostromecki, I. Wachs, S. Kohler, J. Ekerdt, *Catal. Lett.* 33 (1995) 209–215.
- [63] G.Q. Wang, W. Lan, M.L. Yu, G.J. Han, Y. Wang, Q. Su, X.Q. Liu, *J. Mater. Sci. Mater. Electron.* 22 (2011) 463–466.
- [64] G. Lu, X. Li, Z. Qu, Q. Zhao, H. Li, Y. Shen, G. Chen, *Chem. Eng. J.* 159 (2010) 242–246.
- [65] R.M. Pittman, A.T. Bell, *J. Phys. Chem.* 97 (1993) 12178–12185.
- [66] J.M. Jehng, I.E. Wachs, *J. Phys. Chem.* 95 (1991) 7373–7379.
- [67] H. Zhang, J. Han, X. Niu, X. Han, G. Wei, W. Han, *J. Mol. Catal. A* 350 (2011) 35–39.
- [68] T. Onfroy, G. Clet, S.B. Bukallah, T. Visser, M. Houalla, *Appl. Catal. A* 298 (2006) 80–87.
- [69] J.M. Jehng, I.E. Wachs, *J. Mol. Catal.* 67 (1991) 369–387.
- [70] V. Lebarbier, G. Clet, M. Houalla, *J. Phys. Chem. B* 110 (2006) 22608–22617.
- [71] M.A. Vuurman, I.E. Wachs, A.M. Hirt, *J. Phys. Chem.* 95 (1991) 9928–9937.
- [72] <http://www.xpsfitting.com/>.
- [73] A. Froideval, C. Degueldre, C.U. Segre, M.A. Pouchon, D. Grolimund, *Corros. Sci.* 50 (2008) 1313–1320.
- [74] V.A. Shuvaeva, Y. Azuma, I.P. Raevski, K. Yagi, K. Sakaue, H. Terauchi, *Ferroelectrics* 299 (2004) 103–108.
- [75] K. Kato, S. Tamura, *Acta Cryst. B* 31 (1975) 673–677.
- [76] B.M. Gatehouse, A.D. Wadley, *Acta Cryst.* 17 (1964) 1545–1554.
- [77] S. Yamazoe, Y. Hitomi, T. Shishido, T. Tanaka, *J. Phys. Chem. C* 112 (2008) 6869–6879.
- [78] P. Charton, L. Gengembre, P. Armand, *J. Solid State Chem.* 168 (2002) 175–183.
- [79] F. Hilbrig, H.E. Gobel, H. Knozinger, H. Schmelz, B. Lengeler, *J. Phys. Chem.* 95 (1991) 6973–6978.
- [80] J.A. Horsley, I.E. Wachs, J.M. Brown, G.H. Via, F.D. Hardcastle, *J. Phys. Chem.* 91 (1987) 4014–4020.
- [81] S. Tanisaki, *J. Phys. Soc. Jpn.* 15 (1960) 573–581.
- [82] G. Busca, H. Saussey, O. Saur, J.C. Lavalley, V. Lorenzelli, *Appl. Catal.* 14 (1985) 245–260.
- [83] A. Gutiérrez-Alejandre, M. Trombetta, G. Busca, J. Ramírez, *Microporous Mater.* 12 (1997) 79–91.
- [84] G. Busca, V. Lorenzelli, G. Ramis, R.J. Willey, *Langmuir* 9 (1993) 1492–1499.
- [85] M. Bevilacqua, T. Montanari, E. Finocchio, G. Busca, *Catal. Today* 116 (2006) 132–142.
- [86] A. Gutiérrez-Alejandre, P. Castillo, J. Ramírez, G. Ramis, G. Busca, *Appl. Catal. A* 216 (2001) 181–194.
- [87] G. Busca, *Catal. Today* 41 (1998) 191–206.
- [88] G. Busca, *Chem. Rev.* 110 (2010) 2217–2249.
- [89] P.F. Rossi, G. Busca, V. Lorenzelli, M. Waqif, O. Saur, J.C. Lavalley, *Langmuir* 7 (1991) 2677–2681.
- [90] J.C. Lavalley, *Catal. Today* 27 (1996) 377–401.
- [91] G. Busca, V. Lorenzelli, *Mater. Chem.* 7 (1982) 89–126.
- [92] C. Morterra, G. Cerrato, C. Emanuel, *Mater. Chem. Phys.* 29 (1991) 447–456.
- [93] G. Ramis, G. Busca, C. Cristiani, L. Lietti, P. Forzatti, F. Bregani, *Langmuir* 8 (1992) 1744–1749.
- [94] J. Sohn, J. Bae, *Korean J. Chem. Eng.* 17 (2000) 86–92.
- [95] M. Sundberg, *Acta Cryst. B* 32 (1976) 2144–2149.
- [96] J.-M. Jehng, I.E. Wachs, *Catal. Today* 8 (1990) 37–55.
- [97] Y.J. Pagán-Torres, J.M.R. Gallo, D. Wang, H.N. Pham, J.A. Libera, C.L. Marshall, J.W. Elam, A.K. Datye, J.A. Dumesic, *ACS Catal.* 1 (2011) 1234–1245.
- [98] C. Martín, G. Solana, P. Malet, V. Rives, *Catal. Today* 78 (2003) 365–376.
- [99] X.-F. Yu, N.-Z. Wu, H.-Z. Huang, Y.-C. Xie, Y.-Q. Tang, *J. Mater. Chem.* 11 (2001) 3337–3342.
- [100] I.E. Wachs, T. Kim, E.I. Ross, *Catal. Today* 116 (2006) 162–168.
- [101] T. Kim, A. Burrows, C.J. Kiely, I.E. Wachs, *J. Catal.* 246 (2007) 370–381.

- [102] J.P. Brunelle, *Pure Appl. Chem.* 50 (1978) 1211–1229.
- [103] G.A. Parks, *Chem. Rev.* 65 (1965) 177–198.
- [104] A. Ogundipe, J. Pavlov, W. Braidia, A. Koutsospyros, G. Sen, C. Christodoulatos, G. O'Connor, *Global Nest J.* 11 (2009) 308–317.
- [105] J.M. Jehng, I.E. Wachs, *J. Raman Spectrosc.* 22 (1991) 83–89.
- [106] G. Busca, *Phys. Chem. Chem. Phys.* 1 (1999) 723–736.
- [107] D. Stosic, S. Bennici, J.-L. Couturier, J.-L. Dubois, A. Auroux, *Catal. Commun.* 17 (2012) 23–28.
- [108] W. Suprun, M. Lutecki, R. Glaeser, H. Papp, *J. Mol. Catal. A* 342–343 (2011) 91–100.
- [109] Y.T. Kim, K.-D. Jung, E.D. Park, *Appl. Catal. B* 107 (2011) 177–187.
- [110] B. Katryniok, S. Paul, M. Capron, C. Lancelot, V. Belliere-Baca, P. Rey, F. Dumeignil, *Green Chem.* 12 (2010) 2273–2273.
- [111] A.K. Kinage, P.P. Upare, P. Kasinathan, Y.K. Hwang, J.-S. Chang, *Catal. Commun.* 11 (2010) 620–623.
- [112] L.-Z. Tao, S.-H. Chai, Y. Zuo, W.-T. Zheng, Y. Liang, B.-Q. Xu, *Catal. Today* 158 (2010) 310–316.
- [113] H. Atia, U. Armbruster, A. Martin, *Appl. Catal. A* 393 (2011) 331–339.
- [114] M.A. Reiche, T. Burgi, A. Baiker, A. Scholz, B. Schnyder, A. Wokaun, *Appl. Catal. A* 198 (2000) 155–169.
- [115] V.M. Benitez, C.A. Querini, N.S. Figoli, *Appl. Catal. A* 252 (2003) 427–436.
- [116] A. Erdohelyi, R. Nemeth, A. Hancz, A. Oszko, *Appl. Catal. A* 211 (2001) 109–121.
- [117] B. Katryniok, S. Paul, V. Belliere-Baca, P. Rey, F. Dumeignil, *Green Chem.* 12 (2010) 2079–2098.
- [118] J.M. Clacens, Y. Pouilloux, J. Barrault, *Appl. Catal. A* 227 (2002) 181–190.
- [119] C.L. Lima, S.J.S. Vasconcelos, J. Mendes Filho, B.C. Viana, M.G.C. Rocha, P. Bargiela, A.C. Oliveira, *Appl. Catal. A* 399 (2011) 50–62.